The Astrophysical Journal, 1000:215 (16pp), 2026 April 1 https://doi.org/10.3847/1538-4357/ae448b

Resolved Dust Emission and CO Isotopologues in Giant Molecular Clouds of the Andromeda Galaxy

Chloe Bosomworth[1,2], Jan Forbrich[1,2], Charles J. Lada[2], and Glen Petitpas[3]
[1] Centre for Astrophysics Research, University of Hertfordshire, College Lane, Hatfield AL10 9AB, UK
[2] Center for Astrophysics, Harvard & Smithsonian, 60 Garden St., MS 72, Cambridge, MA 02138, USA
[3] Kavli Institute for Astrophysics and Space Research, Massachusetts Institute of Technology, Cambridge, MA 02139, USA
Received 2025 July 17; revised 2026 January 27; accepted 2026 February 9; published 2026 March 24

Abstract

Dust emission at submillimeter wavelengths can be used to reliably trace the basic properties of molecular clouds. Early results from a recent Submillimeter Array (SMA) survey of the Andromeda galaxy (M31) include the first detections of resolved dust continuum emission from individual giant molecular clouds (GMCs) in an external spiral galaxy. This paper updates the now-complete SMA survey of 80 Herschel-identified giant molecular associations in M31. The SMA survey simultaneously probes dust continuum emission at 230 GHz and the $J = 2 \rightarrow 1$ transitions of the CO isotopologues ^{12}CO, ^{13}CO, and C^{18}O at a spatial resolution of $\lesssim$15 pc. Dust continuum emission was detected in 71 cloud cores, of which 26 were resolved. This more than doubles the size of the previous sample. By comparing dust and CO observations with identical astrometry, we directly measure the dust mass-to-light ratios, $\alpha'_{^{12}\mathrm{CO}}$, and $\alpha'_{^{13}\mathrm{CO}}$. We derive $<\alpha'_{^{12}\mathrm{CO}}> = 0.070 \pm 0.031\, M_\odot\,(\mathrm{K\,km\,s^{-1}\,pc^2})^{-1}$ and $<\alpha'_{^{13}\mathrm{CO}}> = 0.37 \pm 0.20\, M_\odot\,(\mathrm{K\,km\,s^{-1}\,pc^2})^{-1}$ for the increased sample, which are in agreement with previously reported values. From virial analysis, we find that 80% of the GMC regions traced by resolved dust emission are bound and close to virial equilibrium. Finally, we update our analysis on the metallicity dependence of α'_{CO} by combining SMA observations with existing MMT/Hectospec optical spectroscopy toward H II regions. We find no trend in α'_{CO} with metallicity, supporting the previous findings.

Unified Astronomy Thesaurus concepts: Interstellar medium (847); Giant molecular clouds (653); Andromeda Galaxy (39); Dust continuum emission (412); Millimeter astronomy (1061); CO line emission (262); Star formation (1569)

Materials only available in the online version of record: figure set, machine-readable tables

1. Introduction

Giant molecular clouds (GMCs) are the main sites of star formation. The physical conditions within GMCs determine the star formation rate (SFR), the primary metric for studies of galaxy (e.g., A. Saintonge & B. Catinella 2022) and cosmic (e.g., P. Madau & M. Dickinson 2014; L. J. Tacconi et al. 2020) evolution. Molecular gas provides the fuel for star formation, and the most abundant molecule in the cold interstellar medium (ISM), which is largely contained within GMCs, is molecular hydrogen (H_2), making up 75% of the mass. Additionally, GMCs are composed of approximately 24% atomic helium (He) and 1% interstellar dust by mass (A. Saintonge & B. Catinella 2022). Both H_2 and He are difficult to detect at the cold temperatures typical of GMCs; therefore, we rely on rarer molecules to detect and probe the molecular gas. In particular, CO is primarily used in extragalactic studies (see, e.g., A. D. Bolatto et al. 2013 for a review) because it emits the strongest molecular emission lines in cold GMCs. However, CO only accounts for ∼0.03% of GMC mass (e.g., M. Heyer & T. Dame 2015), is optically thick in dense cloud regions due to its high opacity, and depletes onto dust grains. As a result, CO traces the diffuse GMC envelopes and does not reflect the denser regions of the cloud. Dense gas is key to understanding global star formation efficiency and the SFR (Y. Gao & P. M. Solomon 2004; C. J. Lada et al. 2010, 2012), so it is vital to investigate alternative tracers that better probe the physical properties of clouds.

Observations of dust extinction in Milky Way (MW) GMCs have provided detailed information on cloud structure as well as the first robust measurements of GMC masses (e.g., C. J. Lada et al. 1994, 2010; J. Alves et al. 2001; A. A. Goodman et al. 2009). Dust is ∼30× more abundant than CO in GMCs, and since molecules such as H_2 and CO form on the surface of dust grains (e.g., V. Wakelam et al. 2017), it is well mixed with molecular gas. At submillimeter wavelengths, we can probe thermal dust continuum emission, which traces H_2 gas properties more accurately than CO due to its lower optical depth (e.g., N. Scoville et al. 2016, 2017). Although dust extinction measurements are independent of dust temperature (T_{dust}), dust emission depends on T_{dust} and opacity (κ_ν). However, unlike molecular excitation lines, dust emission does not depend on excitation conditions.

To fully understand the star formation processes and conditions in a galaxy, we need to probe GMCs across the entire disk of the galaxy. This is difficult in the MW because of distance measurement uncertainties and line-of-sight dust extinction, particularly for clouds located near the center of the galaxy. GMCs within an external galaxy are approximately the same distance from us; therefore, we can obtain a large sample of measurements at a consistent resolution. As the most easily observable tracer, CO is primarily used to trace molecular gas in extragalactic GMCs. The first resolved CO detections of extragalactic GMCs were made in the

Andromeda galaxy (S. N. Vogel et al. 1987; C. J. Lada et al. 1988). More recently, resolved observations of extragalactic GMCs in CO on ∼100 pc scales (e.g., PHANGS-ALMA; A. K. Leroy et al. 2021) and ∼10 pc scales (e.g., D. Colombo et al. 2014; C. M. Faesi et al. 2018) have become routine.

Herschel studies reveal the spatial distribution of giant molecular associations (GMAs) in M31, traced by dust emission at ∼93 pc spatial resolution (J. Fritz et al. 2012; J. M. Kirk et al. 2015). These GMAs have sizes of ∼80–300 pc, thus typically encompass associations of multiple unresolved GMCs. Generally, GMCs have sizes of ∼20–100 pc (P. M. Solomon et al. 1979), which means that individual GMCs are not resolved by Herschel. Extragalactic studies of resolved GMCs are predominantly limited to CO due to the high sensitivity required to detect and resolve dust emission from extragalactic GMCs. This changed with the recent wideband sensitivity upgrade of the Submillimeter Array (SMA; P. Grimes et al. 2016), which has enabled the first resolved dust emission detections from GMCs in an external spiral galaxy, M31, at $\lesssim$15 pc (J. Forbrich et al. 2020; S. Viaene et al. 2021).

To detect resolved dust continuum from individual GMCs in M31, long exposure times were required. Therefore, observing the entire galaxy would be extremely difficult, and as a result, a sample of targets was selected from the HELGA dust continuum survey of Herschel-identified GMAs (J. M. Kirk et al. 2015). The aforementioned SMA survey obtained simultaneous dust emission and three CO isotopologues, ^{12}CO(2−1), ^{13}CO(2−1), and C^{18}O(2−1), with identical *uv*-coverage, spatial scales, and calibration (see J. Forbrich et al. 2020; S. Viaene et al. 2021; C. J. Lada et al. 2024). Since M31 GMCs have an approximately uniform distance from us (∼780 kpc; K. Z. Stanek & P. M. Garnavich 1998), this dust survey has the advantage of eliminating significant uncertainties in the distance measurements present in MW studies.

Two previous papers report 32 dust continuum detections (10 resolved) associated with M31 GMCs from the analysis of the first two observing runs of an SMA large survey (J. Forbrich et al. 2020; S. Viaene et al. 2021). In this paper, we present the updated analysis of the now-completed survey after four observing runs, increasing the sample size to 71 dust continuum detections (26 resolved). The sensitivity of these observations enabled resolved dust emission detections on scales of ∼15 pc. Since the sensitivity to dust in these observations is not sufficient to trace entire GMCs, individual dust detections are hereafter referred to as "dust cores" (following S. Viaene et al. 2021). The sensitivity achieved in ^{12}CO enables measurement of the full ^{12}CO(2–1) emitting area of each GMC (S. Viaene et al. 2021), allowing us to identify the dust emission associated with these clouds.

From CO and dust emission in the same clouds, we can directly calculate $\alpha'_{\rm CO}$, the ratio between dust mass ($M_{\rm dust}$) and CO luminosity ($L_{\rm CO}$). This ratio is related to the CO-to-H_2 conversion factor, $\alpha_{\rm CO}$, through the gas-to-dust ratio ($R_{\rm g/d}$). Therefore, calculating $\alpha_{\rm CO}$ requires an assumption of $R_{\rm g/d}$, for which the typical MW value is $R_{\rm g/d} \sim 136$ (including a factor of 1.36 to account for He; B. T. Draine et al. 2007). However, chemical evolution models (e.g., L. Mattsson & A. C. Andersen 2012; H. Hirashita & N. Harada 2017) and observations (e.g., K. M. Sandstrom et al. 2013; A. Giannetti et al. 2017) have shown that $R_{\rm g/d}$ can vary with dust grain size and metallicity. By measuring $\alpha'^{12}_{\rm CO}$ and $\alpha'^{13}_{\rm CO}$ independently of $R_{\rm g/d}$, we exploit the full capability of dust as a molecular gas tracer and gain insight into the ISM conditions of star formation directly from these observations. Moreover, by deriving $\alpha'_{\rm CO}$ for both the ^{12}CO and the rarer CO isotopologue ^{13}CO in the same sources, we can compare molecular gas components with different opacities.

The combination of CO and dust continuum emission observations with identical astrometry enables the calculation of both the luminous and virial masses of these dust cores. C. J. Lada et al. (2024) evaluate the Larson paradigm, which states that GMCs are in dynamical equilibrium with gravity, for a sample of 117 GMCs in M31. Using data from the same SMA survey described in this work and employing ^{12}CO(2−1) to trace cloud boundaries, Lada et al. found that this paradigm does not hold for most M31 GMCs. In contrast, for the dense regions of GMCs traced by ^{13}CO emission in these observations, the majority were found to be gravitationally self-bound. These ^{13}CO detections are referred to as "clumps" because they, like dust, do not trace entire GMCs, and a single GMC can have multiple associated clumps. In this paper, we assess the virial state of resolved dust cores, which are constrained to the dense regions of GMCs in our observations.

The accuracy of CO as a molecular gas tracer depends on correctly accounting for the effects of metallicity on CO abundance and conversion factors. CO conversion factors, $X_{\rm CO}$ and $\alpha_{\rm CO}$, are predicted to vary with metallicity (e.g., A. K. Leroy et al. 2011; A. D. Bolatto et al. 2013). At lower metallicities, less carbon (C) and oxygen (O) are available, resulting in lower CO abundance (P. Maloney 1988; F. P. Israel 1997). Therefore, $L_{\rm CO}$ per unit gas mass is predicted to decrease at lower metallicities. Furthermore, approximately 30%–50% of metals are expected to deplete onto dust grains (B. D. Savage & K. R. Sembach 1996; B. T. Draine et al. 2007), so $M_{\rm dust}$ and dust opacity also increase with metallicity. Dust extinction shields H_2 and CO molecules from photodissociation by UV radiation.

Therefore, more effective dust shielding at higher metallicities allows CO to trace a larger fraction of the molecular gas (e.g., S. C. O. Glover et al. 2010; S. C. O. Glover & P. C. Clark 2012). The metallicity dependence of $\alpha'_{\rm CO}$ provides insight into the relative effects of metallicity on $M_{\rm dust}$ and $L_{\rm CO}$ and how this in turn could affect $\alpha_{\rm CO}$ if $R_{\rm g/d}$ is assumed to be constant. In C. Bosomworth et al. (2025), an approximately constant $\alpha'^{12}_{\rm CO}$ was found across the metallicity range $12 + \log({\rm O/H}) = 8.4$–$8.7$. A possible explanation for this behavior is that the simultaneous effects on $M_{\rm dust}$ and $L_{\rm CO}$ may cancel out at these metallicities. By comparing our $\alpha'^{12}_{\rm CO}$ values from the updated dust core sample with gas-phase oxygen abundance measurements (O/H) of individual H II regions associated with a subset of these GMCs, we update the result presented in C. Bosomworth et al. (2025). This allows us to further constrain the metallicity dependence of $\alpha'_{\rm CO}$.

This paper is structured as follows. In Section 2, we describe our SMA observations and the selection of our target sources. In Section 3, we outline our methodology and data analysis procedures. In Section 4, we present the results of our analysis, including $L_{\rm CO(2-1)}$ for both ^{12}CO and ^{13}CO, along with the corresponding values of $M_{\rm dust}$ and $\alpha'_{\rm CO}$. Additionally, we perform a virial analysis of the dust cores and investigate the metallicity dependence of $\alpha'^{12}_{\rm CO}$. Finally, in Section 5, we present our summary and conclusions.

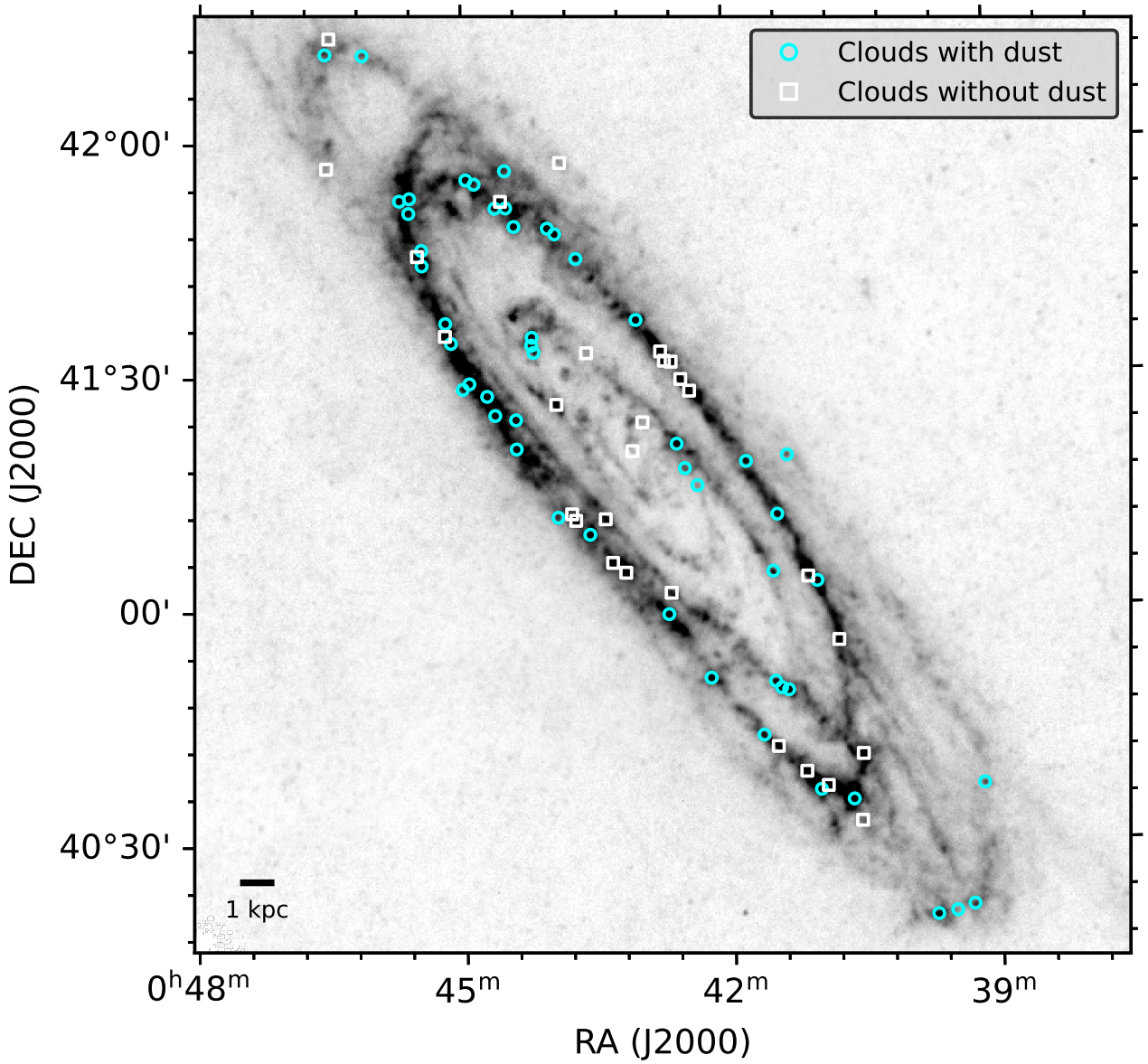

Figure 1. Locations of SMA-observed GMAs (J. M. Kirk et al. 2015) overplotted onto the Herschel Spectral and Photometric Imaging Receiver 500 μm image (J. Fritz et al. 2012), with GMAs for which we obtained dust detections displayed as open circles and GMAs observed but with no dust detections displayed as open squares. The 1 kpc scale bar assumes the distance to M31 to be 780 kpc (K. Z. Stanek & P. M. Garnavich 1998).

2. Observations

Observations were obtained from an SMA large program targeting individual resolved GMCs in M31. This survey used the SMA in the subcompact configuration, which achieved a synthesized beam size of $4\farcs5 \times 3\farcs8$ (~15 pc). Occasionally, one or two antennas were out of service due to technical issues, which increased the typical beam size to $\sim 8'' \times 5''$ ($\sim 30 \times 19$ pc), still sufficient to resolve individual GMCs. At a frequency of 230 GHz (1.3 mm), the bandwidth was 32 GHz for the first two observing runs and subsequently increased to 48 GHz for the final two runs. Within this frequency range, we have access to thermal dust continuum emission and the ^{12}CO(2−1), ^{13}CO(2−1), and C^{18}O(2−1) molecular lines. Analysis and results from the first two observing runs are presented by J. Forbrich et al. (2020) and S. Viaene et al. (2021).

As the entire galaxy could not be observed within a reasonable time frame, targets were selected from the HELGA dust continuum survey of Herschel-identified GMAs (J. M. Kirk et al. 2015). The targets were chosen to cover a representative range of Herschel fluxes and physical cloud properties present throughout the M31 disk. Toward the beginning of the survey, it was found that the likelihood of detecting dust continuum emission on ~15 pc scales was not strongly correlated with Herschel flux on ~100 pc scales, nor was it dependent on position within the disk (J. Forbrich et al. 2020). The spatial distribution of the SMA-observed GMAs across M31 is displayed in Figure 1, overlaid on the Spitzer MIPS infrared 24 μm image (K. D. Gordon et al. 2006). These observations produced dust detections from GMCs distributed across the disk of M31, spanning a wide range of galactocentric radii and Herschel fluxes.

Data were collected from 100 pointings toward 80 targets over four fall seasons from 2019 to 2022. Each source was observed for ~6 hr, and the target sensitivity of 0.20 mJy beam^{-1} to the dust continuum was consistently achieved. The typical rms values reached for the ^{12}CO(2−1) and ^{13}CO(2−1) molecular

lines are, respectively, 20 and 14 mJy beam^{-1} (0.04 and 0.03 K) per $\sim\Delta 1$ km s^{-1} channel. We obtained dust continuum detections associated with GMCs for 51 of the targeted GMAs. A typical resolution of $\sim$15 pc was achieved. Two receivers were used, RxA and RxB, tuned to local oscillator frequencies of 225.55 and 233.55 GHz, respectively. This provided a CO resolution of 140.0 kHz channel^{-1} and, initially, a continuous bandwidth between 213.55 and 245.55 GHz. Within this frequency range, the emission lines ^{12}CO(2−1), ^{13}CO(2−1), and C^{18}O(2−1) are accessible. Subsequently, the coverage was extended to 48 GHz, providing continuous coverage between 209.5 and 249.5 GHz, with an overlap of 8 GHz.

These data were obtained in the form of spectral cubes, from which the CO-contaminated channels were extracted and analyzed using the Millimeter Interferometer Reduction IDL software for the SMA. Continuum images were computed from the average of the remaining channels. For ^{12}CO(2−1) and ^{13}CO(2−1), integrated-intensity (moment 0) maps were produced, as well as data cubes containing the corresponding velocity information. Raw spectra were binned to a velocity resolution of either 1 or 1.5 km s^{-1}. Additional spectral flagging, inversion, and CLEANing were performed in Miriad.[4] For detailed data calibration and reduction procedures, we refer the reader to J. Forbrich et al. (2020).

3. Methodology

In this section, we outline the extraction of thermal dust emission detections from the continuum images and refine the final sample used in further analysis. The sample presented here includes those previously reported in S. Viaene et al. (2021), along with new observations and updated measurements obtained using the methodology outlined below. We make use of both dust continuum images and CO moment 0 maps to ensure that our detected dust continuum cores are associated with GMCs. In addition, CO velocity information is used to extract spectral line profiles for $L_{\rm CO}$ measurements. For the analysis of GMCs and ^{13}CO clumps, as defined by their CO emission contours from this same dataset, we refer to C. J. Lada et al. (2024).

3.1. Dust Core Extraction

To identify and extract individual GMCs and dust cores from each observation, we define contours based on the image rms, σ. The high sensitivity achieved in the ^{12}CO(2−1) data means that the 3σ contours typically trace the entire CO-emitting area of each GMC (S. Viaene et al. 2021). Because the dust continuum images and CO moment 0 maps have identical astrometry, we no longer depend on the global image statistics to identify dust continuum emission. Instead, we perform a targeted search within the GMC boundaries. We employ a 2.5σ detection threshold, lower than the 3σ threshold used by J. Forbrich et al. (2020) and S. Viaene et al. (2021). A 2.5σ threshold improves our sensitivity to dust emission compared to previous analyses and introduces only minimal contamination from unrelated foreground or background sources. Applying this criterion to the entire survey, including the observations previously analyzed by J. Forbrich et al. (2020) and S. Viaene et al. (2021), more than doubles the size of the previous sample.

[4] cfa.harvard.edu/sma/miriad/

At the achieved sensitivity, dust emission and ^{13}CO do not trace the entire extent of each GMC, and we find that a single GMC can have multiple associated dust cores and ^{13}CO clumps. Dust continuum emission at the 2.5σ level was detected in 35 targeted GMAs associated with 57 separate GMCs. Compared to the previous sample from S. Viaene et al. (2021), the complete sample of dust cores has increased from 32 to 71, and the number of resolved cores has increased from 10 to 26.

We define a resolved core as one that has a 2.5σ contour at least 20% larger than the synthesized beam and analyze these separately from the unresolved sources. This allows us to evaluate the extent to which measurements may be affected by differences in the beam-filling factors of CO and dust. Finally, pixels outside the half-power primary beam ($r = 27\farcs5$, or $\sim$100 pc) are removed, except for source K098Bd1, where we find a resolved dust detection associated with a GMC whose dust and CO contours both partially overlap the edge of the half-power primary beam.

3.2. Dust Mass Measurements

To calculate the dust mass of an individual core, $M_{\rm dust}$, we use the modified blackbody emission model of R. H. Hildebrand (1983):

$$M_{\rm dust} = \frac{S_\nu D^2}{\kappa_\nu B_\nu(T_{\rm dust})}. \quad (1)$$

Here, $D = 780$ kpc (K. Z. Stanek & P. M. Garnavich 1998), and S_ν is the continuum flux density measured within the 2.5σ contour. We adopt a dust opacity of $\kappa_\nu = 0.0425$ m^2 kg^{-1} from the THEMIS dust model (A. Jones et al. 2017) at 230 GHz, which has been calibrated using Planck data and the MW dust constraints of N. Ysard et al. (2015). This dust model has previously been shown to perform well in radiative transfer modeling of M31 by S. Viaene et al. (2017). Finally, we assume a dust temperature of $T_{\rm dust} = 18$ K, the median value derived for the J. M. Kirk et al. (2015) GMAs.

To measure $M_{\rm dust}$ from our continuum images, we must first calculate S_ν for each dust core. For resolved sources, we calculate the average flux from all pixels within the 2.5σ contour and multiply this value by the source area (in pixels) to obtain S_ν. For unresolved sources, we use the peak pixel flux and multiply it by the beam area (in pixels).

There is a possible uncertainty associated with the assumption of a constant dust temperature; therefore, the magnitude of this effect was previously assessed by S. Viaene et al. (2021). By assuming constant dust temperatures of $T_{\rm dust} = 15$ K and $T_{\rm dust} = 25$ K (the range of dust temperatures found for GMAs studied by J. M. Kirk et al. 2015) in the dust mass calculations, S. Viaene et al. (2021) found that a $\pm$5 K variation in dust temperature does not significantly affect the results.

3.3. CO Luminosity Measurements

To calculate the CO luminous mass, $M_{\rm lum}$, we use CO line profiles extracted from the same regions of each GMC as the dust emission. We extract line profiles for ^{12}CO(2−1) and ^{13}CO(2−1) over a 100 km s^{-1} wide band, centered on the line peak and computed within the boundaries of each individual dust core. In the case of resolved dust cores, we extract the mean line profile of all pixels within the 2.5σ dust core boundary. For unresolved dust cores, we instead use the line

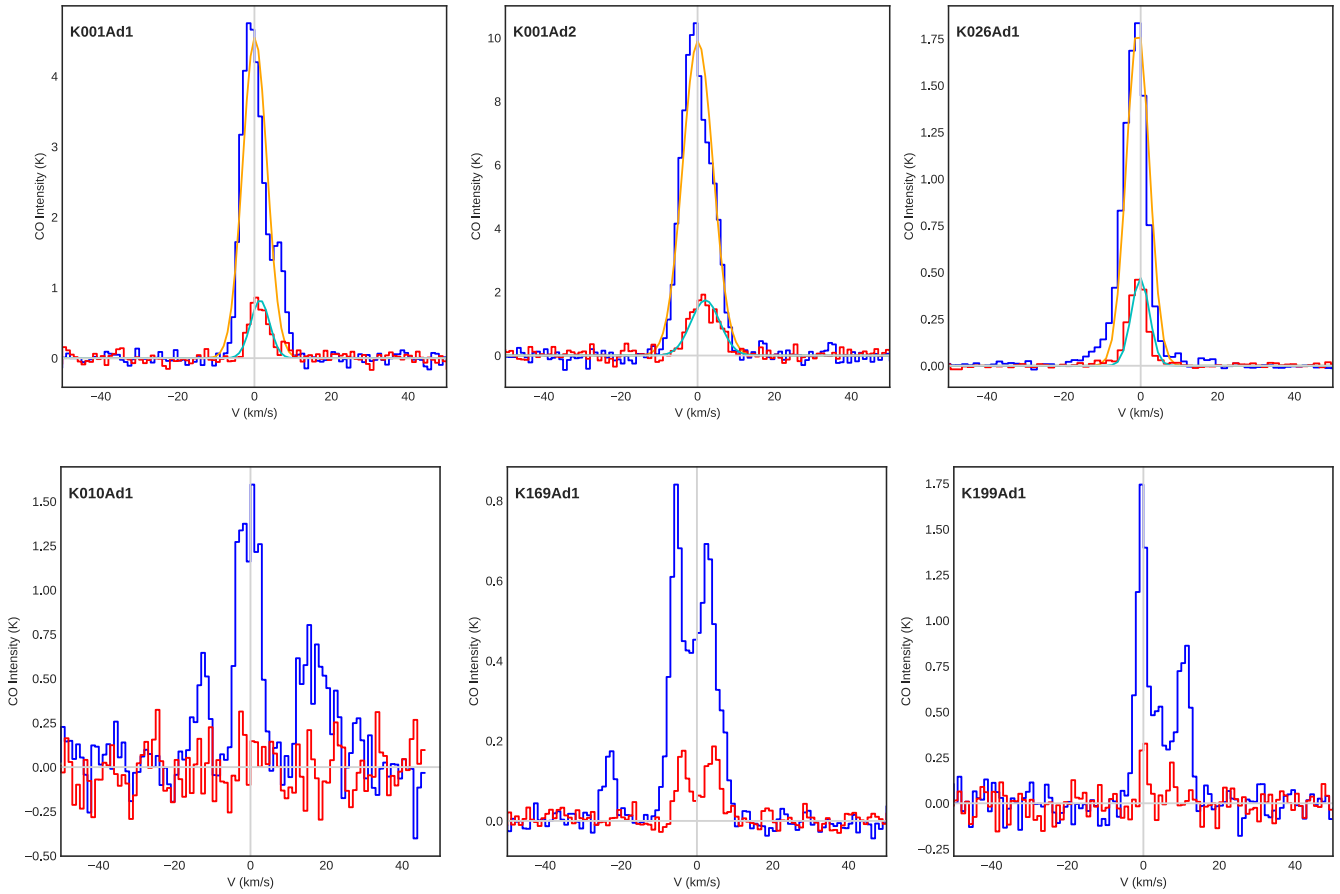

Figure 2. CO line profiles for six individual dust cores. The top panels show three dust cores from the 1G sample, while the bottom panels show three dust cores with multiple-component CO line profiles. Both ^{12}CO and ^{13}CO spectral lines are displayed with the corresponding Gaussian fits.

profile of the peak pixel within the contour. Line profiles are well resolved in velocity, and their line widths are comparable to those of MW GMCs (e.g., ∼4–6 km s^{-1}; T. S. Rice et al. 2016), except for source K008, which contains two dust cores with extracted ^{12}CO line widths of ∼18 and ∼31 km s^{-1}. The CO intensity, $I_{\rm CO}$, of each dust core is measured from a Gaussian fit to the line profile. We then calculate $L_{\rm CO}$ following Equation (2),

$$L_{\rm CO} = I_{\rm CO} \times A_{\rm source}\,, \tag{2}$$

where $A_{\rm source}$ is in pixels and corresponds to the 2.5σ contour area for resolved sources and the beam area for unresolved sources.

Previous $L_{\rm CO}$ measurements reported by J. Forbrich et al. (2020) and S. Viaene et al. (2021) were derived from moment 0 maps. Unlike the dust emission, our ^{12}CO(2–1) observations are not limited by sensitivity, and the emission is detected in all moment 0 images. Given the strength of the ^{12}CO(2−1) emission, regions of images that are free of ^{12}CO emission are much less common than for dust and ^{13}CO emission. This makes an accurate determination of the ^{12}CO image rms difficult. The updated method used in this work improves the uncertainty estimate for $I_{\rm CO}$, which is calculated following

$$\delta I_{\rm CO} = \sigma_{\rm channel}\ \Delta v\ \sqrt{N_{\rm channel}}\,, \tag{3}$$

where $\sigma_{\rm channel}$ is the rms noise per channel calculated from two 20 km s^{-1} ranges on both sides of the CO line profile, Δv is the channel width (1 or 1.5 km s^{-1}), and N is the number of channels summed over the line profile (FWHM ×2.4). This ratio is multiplied by the dust core area (resolved sources) or the beam area (unresolved sources) to calculate the uncertainty in $L_{\rm CO}$. The image rms is still used to define the 3σ contours for CO emission.

The final sample of dust cores can be further refined based on their respective CO line profiles. The presence of multiple peaks within a line profile indicates that there are multiple sources along the line of sight contributing to the emission in the moment 0 maps and dust continuum images. In these cases, we cannot determine the fraction of dust emission corresponding to each source; therefore, the measured dust properties may not reflect an individual GMC. For this reason, we define a subsample of dust cores with approximately single-Gaussian ^{12}CO and ^{13}CO line profiles (hereafter referred to as "1G," following the terminology of C. J. Lada et al. 2024). This criterion also excludes 12 dust cores for which the ^{13}CO peak is not present in the spectrum. As ^{13}CO is expected to spatially align with the dust emission (see Section 4.1; J. Forbrich et al. 2020; S. Viaene et al. 2021), this further refines our sample to the highest-quality data to ensure reliable measurements. The 1G sample excludes 26 sources (5 resolved) from the full sample, including 15 from the S. Viaene et al. (2021) sample.

In Figure 2, we show CO line profiles for (1) three dust cores from our 1G sample and (2) three dust cores with multiple-component line profiles. We display both ^{12}CO and ^{13}CO line profiles with corresponding Gaussian fits for the 1G sources, from which the CO intensity was measured. The line

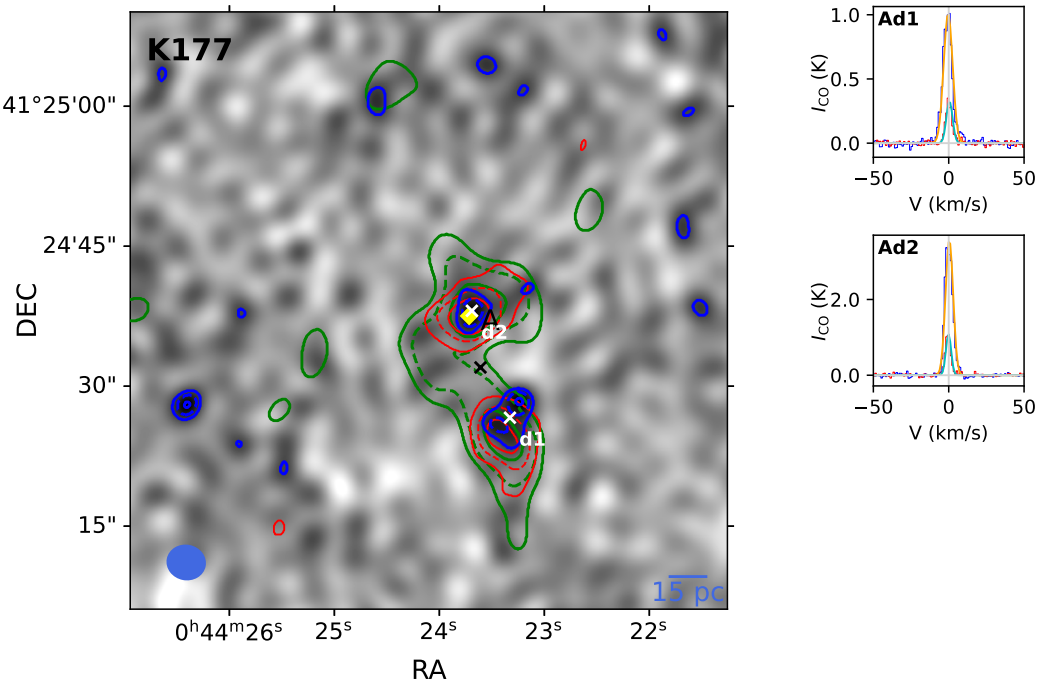

Figure 3. Left: SMA maps of the dust continuum of individual (J. M. Kirk et al. 2015) GMAs in M31 for fields that contain one or more dust cores. Blue contours display dust continuum emission at 2.5σ, 3.5σ, and 4.5σ, where σ is the continuum image background rms, the values given in Table 1. Green contours display ^{12}CO at 3σ, 6σ, 12σ, 24σ, and 48σ. Red contours display ^{13}CO at 3σ, 6σ, and 10σ. The corresponding center of mass (by area) of individual GMCs as traced by ^{12}CO at 3σ are marked by black crosses, and individual dust cores as traced by dust continuum at 2.5σ are marked by white crosses. Right: corresponding CO line profiles extracted from within individual dust cores for both ^{12}CO and ^{13}CO. Hectospec fiber positions corresponding to H II regions identified from optical spectroscopy (C. Bosomworth et al. 2025) and associated with GMCs hosting a 1G dust core are shown as yellow diamonds (see Section 4.5). Gaussian fits to the line profiles are displayed for the 1G sample.

(The complete figure set (50 images) is available in the online article.)

profiles for the entire dust core sample are displayed in Figure 3, along with the corresponding dust continuum images. CO line profiles extracted from the 1G sources are well represented by a single Gaussian fit. C. J. Lada et al. (2024) calculated formal uncertainties in velocity dispersions and integrated intensities for CO line profiles extracted from this same survey, corresponding to entire GMCs rather than dust cores, as is done in this work. For ^{12}CO, the uncertainties in measurements of line dispersion and intensity are 3% and 8%, respectively. For ^{13}CO, uncertainties of 4% and 15% were found. These relatively small uncertainties highlight the high quality of these spectra. Therefore, we conclude that the uncertainties in these Gaussian fits are likely similar.

4. Results and Discussion

This section presents the results of our analysis of the dust core sample. After applying the methodology to this sample of 71 dust cores, we obtain the size, continuum flux, and L_{CO} for individual detections. We first combine M_{dust} with the corresponding CO(2–1) emission to measure α'_{CO} (i.e., M_{dust}/L_{CO}) for both ^{12}CO and ^{13}CO for all dust cores. For resolved dust cores, we perform a virial analysis to determine whether these are self-bound by gravity and approximately satisfy the virial theorem. Finally, we compare our results to H II region metallicities from C. Bosomworth et al. (2025) to update the direct test on the metallicity dependence of α'_{CO}.

4.1. Dust Continuum Images and CO Line Profiles

Dust continuum images of the 51 observed GMAs containing one or more dust cores are displayed in Figure 3, along with the CO line profiles of any associated dust cores. The GMAs without an associated dust core are displayed in the Appendix. CO contours in Figure 3 correspond to the CO(2–1) moment 0 maps, which have identical astrometry and *uv*-coverage to the continuum images, allowing us to directly compare their spatial extent.

In all maps, ^{12}CO emission is more spatially extended than the ^{13}CO emission, which is in turn more extended than the continuum emission. This indicates that, at the sensitivity of our observations, we detect ^{13}CO and dust continuum emission from the higher column density regions of GMCs, while ^{12}CO traces the entire extent of the molecular cloud. NOEMA images presented by J. Forbrich et al. (2023) show that the dust continuum emission in these observations is spatially similar to HCN and HCO$^+$, both of which have high dipole moments compared to CO and are assumed to trace dense gas (i.e., $n(H_2) \gtrsim 10^4\,cm^{-3}$), indicating that we are probing similarly dense material at the available sensitivity.

4.2. Dust Core Properties

The left panel of Figure 4 displays the dust mass distribution for the entire sample of 71 dust cores, and the right panel shows the dust mass distribution for the 47 1G dust cores only, with the numbers of resolved and unresolved cores displayed separately. These include dust cores previously reported by S. Viaene et al. (2021) but with updated dust masses calculated using the 2.5σ detection threshold, as described in Section 3.2. Resolved dust cores lie primarily in the dust mass range of $M_{dust} \sim$ 200–700 $M_\odot$. The multicomponent sample contains only five resolved sources. By comparing the two histograms in Figure 4, we conclude that the majority of the non-1G sources are

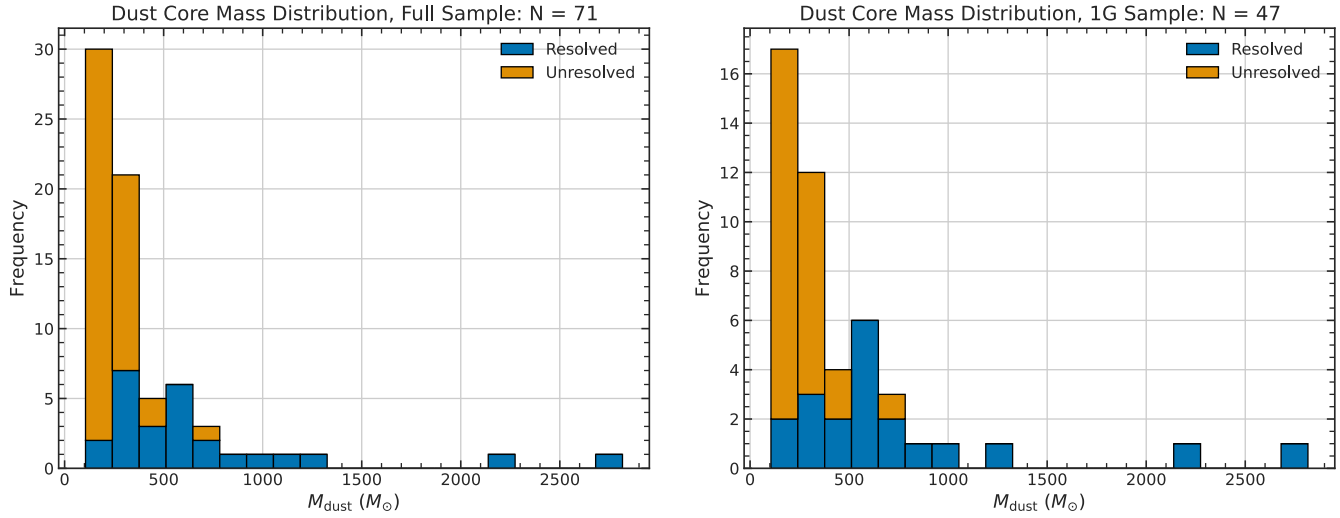

Figure 4. Histogram of dust masses for (left) our full sample of dust cores, of which 26 are resolved and 45 unresolved, and (right) our 1G sample of dust cores, of which 20 are resolved and 27 unresolved.

Table 1
Table of Dust Core Properties

Source	R.A., Decl.[a] J2000	Radius (Deconv.) (pc)	F_{cont} (mJy)	rms (mJy beam^{-1})	Beam Size $a \times b$ (arcsec)	M_{dust} ($M_\odot$)	$I_{^{12}CO}$ (K km s^{-1})	$I_{^{13}CO}$ (K km s^{-1})
K001Ad1	00:39:10.2, +40:37:22.2	7.5	0.9 ± 0.2	0.2	4.4 × 3.4	280 ± 66	28.5 ± 0.2	4.0 ± 0.2
K001Ad2	00:39:09.8, +40:37:16.8	4.8	0.6 ± 0.2	0.2	4.4 × 3.4	207 ± 66	34.9 ± 0.3	5.8 ± 0.2
K008Ad1	00:42:27.2, +41:18:18.8	7.2	0.5 ± 0.1	0.1	4.1 × 3.6	170 ± 40	8.7 ± 0.5	0.2 ± 0.1
K008Ad2	00:42:28.8, +41:18:22.3	4.3	0.3 ± 0.1	0.1	4.1 × 3.6	115 ± 40	30.5 ± 0.3	0.2 ± 0.0
K010Ad1	00:42:34.5, +41:21:09.0	4.6	0.5 ± 0.1	0.1	3.9 × 3.4	158 ± 45	4.1 ± 0.3	0.2 ± 0.1
K026Ad1[b]	00:41:29.7, +41:04:56.2	20.8	4.0 ± 0.4	0.2	4.5 × 4.0	1315 ± 125	13.5 ± 0.1	2.8 ± 0.0
K029Ad1	00:42:20.5, +41:16:02.5	5.1	0.5 ± 0.2	0.2	4.1 × 3.5	177 ± 51	16.4 ± 0.6	0.8 ± 0.2
K060Ad1	00:41:00.1, +40:36:59.2	5.4	0.6 ± 0.2	0.2	4.2 × 3.5	183 ± 60	7.7 ± 0.2	1.4 ± 0.2
K060Ad2	00:40:59.5, +40:36:45.5	4.6	0.5 ± 0.2	0.2	4.2 × 3.5	154 ± 60	1.4 ± 0.2	0.2 ± 0.1
K063Ad1[b]	00:40:40.1, +40:35:40.5	14.1	1.0 ± 0.2	0.1	3.8 × 3.5	325 ± 54	6.7 ± 0.1	0.9 ± 0.1
K063Ad2	00:40:39.2, +40:35:38.9	4.6	0.4 ± 0.1	0.1	3.8 × 3.5	118 ± 32	8.0 ± 0.2	1.0 ± 0.2
K063Ad3	00:40:39.0, +40:35:31.0	4.7	0.3 ± 0.1	0.1	3.8 × 3.5	105 ± 32	12.2 ± 0.3	1.7 ± 0.2
K067Ad1[b]	00:41:38.1, +40:43:56.6	10.1	0.7 ± 0.2	0.2	4.2 × 3.7	213 ± 60	11.0 ± 0.1	2.2 ± 0.1
K071Ad1[b]	00:41:00.8, +41:03:59.4	12.6	1.9 ± 0.3	0.2	4.0 × 3.6	627 ± 115	11.3 ± 0.2	2.4 ± 0.1
K071Ad2	00:41:00.8, +41:03:36.4	4.3	0.8 ± 0.2	0.2	4.0 × 3.6	267 ± 78	23.7 ± 1.3	3.1 ± 0.2
K078Bd1[b]	00:41:28.0, +41:12:06.9	10.1	0.8 ± 0.2	0.2	4.0 × 3.4	248 ± 71	4.4 ± 0.2	0.4 ± 0.1
K081Ad1	00:41:47.4, +41:18:55.2	6.9	0.7 ± 0.2	0.2	4.0 × 3.5	232 ± 66	18.5 ± 0.3	3.7 ± 0.2
K092Ad1[b]	00:41:22.1, +40:49:52.2	18.0	1.6 ± 0.2	0.2	6.9 × 5.0	522 ± 76	5.4 ± 0.1	1.4 ± 0.0
K093Ad1[b]	00:41:25.7, +40:49:55.9	11.7	1.3 ± 0.3	0.2	4.2 × 3.6	427 ± 96	9.2 ± 0.1	2.2 ± 0.4
K094Ad1	00:41:29.2, +40:50:49.6	6.3	0.5 ± 0.2	0.2	4.2 × 3.3	166 ± 56	19.9 ± 0.2	3.5 ± 0.1
K098Ad1	00:43:02.8, +41:37:21.5	5.0	0.7 ± 0.2	0.2	4.0 × 3.6	223 ± 80	19.0 ± 0.3	2.5 ± 0.2
K098Bd1[b]	00:42:59.5, +41:37:07.3	13.4	2.3 ± 0.4	0.2	4.0 × 3.6	746 ± 125	27.4 ± 0.2	5.3 ± 0.2
K119Bd1[b]	00:43:34.4, +41:09:43.9	18.4	3.1 ± 0.3	0.2	3.9 × 3.5	1002 ± 97	8.0 ± 0.1	1.7 ± 0.0
K120Ad1[b]	00:43:55.1, +41:12:06.5	10.2	0.9 ± 0.2	0.2	4.0 × 3.4	280 ± 73	5.0 ± 0.1	1.1 ± 0.1
K121Dd1	00:42:43.3, +40:59:40.5	5.2	0.4 ± 0.1	0.1	3.6 × 3.2	127 ± 38	1.1 ± 0.2	0.3 ± 0.0
K134Ad1	00:44:23.0, +41:49:18.0	8.2	0.9 ± 0.3	0.3	5.5 × 4.7	299 ± 92	8.6 ± 0.2	1.7 ± 0.1
K134Ad2	00:44:23.8, +41:49:28.5	5.6	0.8 ± 0.3	0.3	5.5 × 4.7	250 ± 92	6.0 ± 0.1	0.7 ± 0.1
K136Ad1[b]	00:44:29.6, +41:51:43.8	21.7	3.3 ± 0.3	0.2	4.4 × 3.9	1086 ± 97	10.3 ± 0.4	2.3 ± 0.1
K136Ad2	00:44:31.3, +41:51:53.1	4.3	0.5 ± 0.1	0.2	4.4 × 3.9	173 ± 42	8.6 ± 0.3	1.6 ± 0.1
K138Ad1[b]	00:44:36.9, +41:51:42.6	13.5	2.0 ± 0.2	0.1	3.5 × 3.3	641 ± 69	20.0 ± 0.1	4.0 ± 0.1
K142Ad1	00:44:57.8, +41:55:24.4	8.6	0.8 ± 0.2	0.2	8.1 × 5.0	259 ± 79	0.6 ± 0.1	0.0 ± 0.0
K142Ad2	00:44:56.9, +41:55:20.6	6.6	0.8 ± 0.2	0.2	8.1 × 5.0	246 ± 79	0.6 ± 0.1	0.0 ± 0.0
K143Ad1	00:44:51.2, +41:54:38.7	4.8	0.7 ± 0.2	0.2	4.0 × 3.5	231 ± 67	9.9 ± 0.2	0.9 ± 0.2
K149Ad1	00:45:36.6, +41:51:05.1	8.5	0.6 ± 0.2	0.2	3.9 × 3.5	178 ± 57	11.1 ± 0.2	2.0 ± 0.1
K151Ad1	00:45:27.0, +41:44:26.8	7.6	0.6 ± 0.2	0.2	8.1 × 5.0	200 ± 68	8.4 ± 0.1	0.7 ± 0.1
K153Ad1	00:45:27.5, +41:46:25.8	8.8	0.8 ± 0.2	0.2	8.0 × 4.9	253 ± 66	11.9 ± 0.1	1.4 ± 0.0
K153Ad2	00:45:27.7, +41:46:38.9	5.3	0.6 ± 0.2	0.2	8.0 × 4.9	182 ± 66	9.2 ± 0.1	1.0 ± 0.0
K154Ad1[b]	00:45:36.0, +41:53:00.4	13.4	1.1 ± 0.2	0.1	4.0 × 3.7	347 ± 67	5.1 ± 0.1	0.8 ± 0.0
K157Ad1[b]	00:45:43.7, +41:52:43.9	7.5	0.9 ± 0.2	0.2	4.2 × 3.7	280 ± 58	11.7 ± 0.4	1.9 ± 0.1
K157Bd1	00:45:41.8, +41:52:45.3	11.1	1.0 ± 0.2	0.2	4.2 × 3.7	321 ± 74	6.9 ± 0.2	0.2 ± 0.1

Table 1
(Continued)

Source	R.A., Decl.[a] J2000	Radius (Deconv.) (pc)	F_{cont} (mJy)	rms (mJy beam^{-1})	Beam Size $a \times b$ (arcsec)	M_{dust} ($M_\odot$)	$I_{^{12}CO}$ (K km s^{-1})	$I_{^{13}CO}$ (K km s^{-1})
K157Bd2	00:45:44.8, +41:52:40.8	4.9	0.6 ± 0.2	0.2	4.2 × 3.7	202 ± 58	7.6 ± 0.1	1.1 ± 0.1
K160Ad1	00:45:07.7, +41:34:20.7	10.8	1.0 ± 0.2	0.2	8.1 × 5.0	324 ± 61	6.1 ± 0.1	1.0 ± 0.2
K160Bd1	00:45:09.2, +41:34:33.1	6.5	0.7 ± 0.2	0.2	8.1 × 5.0	229 ± 61	4.0 ± 0.3	0.5 ± 0.1
K160Cd1	00:45:08.6, +41:34:52.8	14.6	1.2 ± 0.2	0.2	8.1 × 5.0	389 ± 61	5.2 ± 0.6	0.6 ± 0.1
K162Ad1[b]	00:45:11.5, +41:36:58.0	14.3	1.4 ± 0.2	0.2	5.2 × 4.3	463 ± 77	23.1 ± 0.5	3.6 ± 0.6
K162Ad2	00:45:10.8, +41:37:08.0	6.7	0.6 ± 0.2	0.2	5.2 × 4.3	208 ± 58	16.6 ± 0.2	2.3 ± 0.4
K169Ad1[b]	00:44:38.2, +41:25:10.9	13.6	1.3 ± 0.2	0.1	3.6 × 3.3	434 ± 65	8.8 ± 0.2	1.7 ± 0.1
K170Ad1[b]	00:44:42.5, +41:27:36.8	15.2	1.7 ± 0.3	0.1	3.5 × 3.2	562 ± 84	15.2 ± 0.3	2.9 ± 0.1
K171Ad1	00:44:55.7, +41:29:14.7	7.4	0.8 ± 0.2	0.2	4.0 × 3.6	252 ± 69	15.5 ± 0.3	3.7 ± 0.2
K174Ad1	00:44:24.2, +41:21:04.8	7.5	0.9 ± 0.2	0.2	3.9 × 3.5	289 ± 56	6.7 ± 0.4	1.2 ± 0.1
K174Cd1	00:44:23.8, +41:20:29.2	4.8	0.7 ± 0.2	0.2	3.9 × 3.5	212 ± 56	4.0 ± 0.2	0.2 ± 0.1
K176Ad1[b]	00:45:00.2, +41:28:32.5	19.3	1.9 ± 0.3	0.2	8.1 × 5.0	624 ± 94	10.4 ± 0.0	1.8 ± 0.3
K177Ad1[b]	00:44:25.0, +41:24:47.9	9.8	0.4 ± 0.1	0.1	3.8 × 3.4	141 ± 35	7.5 ± 0.1	1.7 ± 0.0
K177Ad2	00:44:24.1, +41:24:42.8	7.2	0.4 ± 0.1	0.1	3.8 × 3.4	134 ± 29	18.5 ± 0.1	3.9 ± 0.1
K190Ad1[b]	00:44:30.3, +41:56:29.6	15.0	1.8 ± 0.2	0.2	4.9 × 4.2	598 ± 68	4.6 ± 0.1	0.4 ± 0.0
K191Ad1[b]	00:44:01.5, +41:49:11.2	16.0	6.9 ± 0.8	0.4	4.2 × 3.3	2270 ± 254	34.9 ± 0.4	6.6 ± 1.1
K192Ad1	00:43:55.9, +41:48:22.5	4.9	1.3 ± 0.4	0.3	4.0 × 3.7	411 ± 120	20.0 ± 0.3	4.8 ± 0.3
K199Ad1	00:43:42.0, +41:45:14.7	7.0	0.7 ± 0.2	0.2	4.0 × 3.6	233 ± 61	4.8 ± 0.4	0.5 ± 0.1
K213Ad1[b]	00:42:13.9, +40:51:17.2	22.9	8.6 ± 0.8	0.3	4.3 × 3.7	2816 ± 252	18.5 ± 0.1	3.3 ± 0.1
K238Cd1	00:44:10.8, +41:35:08.4	5.7	0.7 ± 0.2	0.2	7.8 × 4.9	217 ± 79	4.3 ± 0.2	0.4 ± 0.1
K239Ad1[b]	00:44:12.0, +41:34:11.5	15.8	1.1 ± 0.2	0.2	7.8 × 4.9	368 ± 80	1.5 ± 0.0	0.2 ± 0.0
K239Ad2	00:44:12.5, +41:34:07.3	3.4	0.7 ± 0.2	0.2	7.8 × 4.9	215 ± 70	10.6 ± 0.1	1.5 ± 0.2
K240Ad1	00:44:11.8, +41:33:07.4	4.8	0.7 ± 0.2	0.2	4.0 × 3.5	241 ± 72	7.0 ± 0.2	1.0 ± 0.1
K240Bd1	00:44:12.7, +41:33:13.8	4.9	0.7 ± 0.2	0.2	4.0 × 3.5	233 ± 72	7.7 ± 0.2	0.6 ± 0.2
K270Ad1[b]	00:39:18.4, +40:21:53.1	18.4	2.4 ± 0.2	0.1	3.5 × 3.2	787 ± 72	7.9 ± 0.0	1.2 ± 0.0
K270Ad2	00:39:19.3, +40:22:00.8	4.6	0.3 ± 0.1	0.1	3.5 × 3.2	109 ± 29	10.9 ± 0.1	1.5 ± 0.1
K273Bd1[b]	00:39:43.2, +40:20:43.0	11.1	0.9 ± 0.2	0.2	4.0 × 3.5	295 ± 73	0.8 ± 0.2	0.1 ± 0.0
K275Bd1	00:39:30.3, +40:21:09.8	5.4	0.8 ± 0.2	0.2	4.2 × 3.4	266 ± 68	9.5 ± 0.2	1.4 ± 0.1
K291Ad1	00:46:33.3, +42:11:31.5	9.5	1.1 ± 0.2	0.2	4.4 × 3.8	358 ± 66	5.4 ± 0.1	0.6 ± 0.1
K297Ad1	00:46:07.9, +42:11:26.0	15.0	2.1 ± 0.2	0.2	7.8 × 5.0	675 ± 62	12.6 ± 0.1	1.8 ± 0.1
K301Ad1[b]	00:41:19.3, +41:19:47.8	15.4	2.3 ± 0.2	0.1	3.5 × 3.2	755 ± 77	22.1 ± 0.1	4.2 ± 0.1

Notes.
[a] R.A. and decl. give the coordinates of the center of mass of the dust core.
[b] Resolved dust cores.

(This table is available in machine-readable form in the online article.)

unresolved and have $M_{dust} \lesssim 200\,M_\odot$. The remaining dust cores in our sample are resolved, and three have masses of $M_{dust} > 1000\,M_\odot$. From lowest to highest mass, these are identified as K026Ad1, K191Ad1, and K213Ad1.

We present the properties of individual dust cores from our final sample in Table 1, derived as described above. Dust core nomenclature is based on the corresponding J. M. Kirk et al. (2015) GMA, ordered alphabetically from highest to lowest CO mass of the individual GMC associations. We then introduce d1, d2, etc. labels for dust cores, starting with the highest M_{dust} detection associated with a particular GMC. The deconvolved radii of our resolved dust cores range from ∼10 to 23 pc, while the deconvolved radii of the 3σ ^{12}CO contours range from ∼26 to 61 pc, confirming that we do not trace entire GMCs with dust emission.

Despite the identical astrometry, the peaks of CO and dust emission do not always spatially align. One possible explanation, proposed by S. Viaene et al. (2021), is that dust peaks may correspond to hotter dust heated by ongoing star formation at the edges of GMCs and are therefore spatially separated from the cold gas. The possibility that continuum emission originates from an associated H II region and is contaminated by free–free emission has already been investigated by J. Forbrich et al. (2023), who found that at 230 GHz, free–free emission contributes only 6%–23% of the continuum flux for clouds with Very Large Array–detected H II regions.

The relative sensitivity of our observations to different tracers is crucial for understanding the structure of molecular gas in GMCs. Since CO and continuum observations were obtained simultaneously with the same calibration, imaging, and astrometry, experimental offsets are eliminated. From the areas of the 2.5σ contours for dust emission and the 3σ contours for CO, we find that dust traces 10%–60% of the area traced by ^{12}CO and 35%–80% of the area traced by ^{13}CO emission at the sensitivity achieved. The filamentary nature of molecular clouds implies that at these smaller scales, we are probing higher column densities (T. M. Dame & C. J. Lada 2023). Furthermore, dust and ^{13}CO emission from this SMA survey is cospatial with HCN from NOEMA (J. Forbrich et al. 2023), indicating that dust emission is tracing high-volume-density gas, compared to the more diffuse gas traced by ^{12}CO.

HCN is an assumed dense molecular gas tracer, tracing H_2 densities of $\gtrsim 3 \times 10^4\,cm^{-3}$, compared to CO, which traces densities of $\gtrsim 300\,cm^{-3}$ (Y. Gao & P. M. Solomon 2004). However, recent studies suggest that HCN can also be detected at lower densities (J. Pety et al. 2017; T. M. Dame & C. J. Lada 2023). J. Forbrich et al. (2023) found that the dust emission from the SMA discussed in this work and HCN from

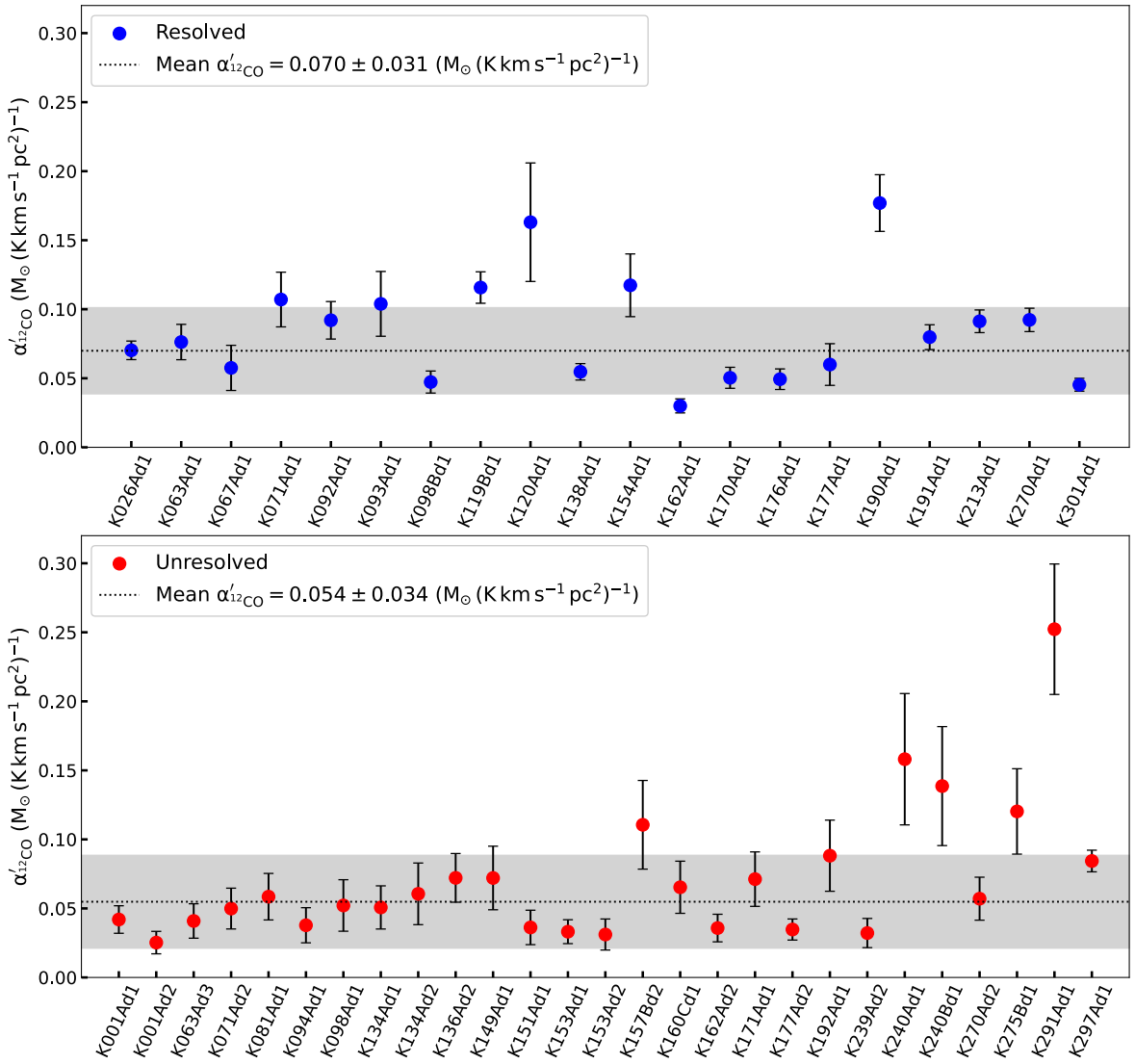

Figure 5. ^{12}CO conversion factors, $\alpha'_{^{12}CO}$, for individual 1G dust cores for (top) resolved sources and (bottom) unresolved sources. We display the mean $\alpha'_{^{12}CO}$ calculated for resolved and unresolved sources as a dotted line, with the 1σ standard deviation represented by the shaded region.

NOEMA observations for a subset of six M31 GMCs are strongly spatially coincident, suggesting that both surveys independently trace the high-column-density gas in the GMCs, reflecting the limited sensitivity. Our observations are therefore consistent with the idea that, at the sensitivity achieved in this study, dust can trace dense molecular gas in GMCs, which is closely related to the SFR (e.g., C. J. Lada et al. 2010, 2012).

4.3. CO Conversion Factors

To convert CO luminosity to cloud mass, we require a conversion factor typically defined as $\alpha_{CO} = M_{tot}/L_{CO}$, where M_{tot} is the total molecular mass of the cloud. Knowledge of the CO conversion factor is critical when dust emission is not detected and only CO is available, such as in distant extragalactic sources. Here, we use dust emission to calibrate α_{CO}. From our observations of dust and CO emission, we can directly measure the dust mass-to-light ratio, α'_{CO}. With an assumed $R_{g/d}$, α'_{CO} can then be converted to α_{CO} by $\alpha_{CO} = \alpha'_{CO} \times R_{g/d}$.

For M31 GMCs, we calculate α'_{CO} for both ^{12}CO(2−1) and ^{13}CO(2−1), denoted as $\alpha'_{^{12}CO}$ and $\alpha'_{^{13}CO}$, respectively. Since in all cases, both values correspond to identical spatial areas, this provides insight into the differences between the two isotopologues as molecular gas tracers. Because ^{12}CO is the most easily observable and often the only tracer available for distant GMCs, calculating $\alpha'_{^{13}CO}$ for the same sources allows us to assess potential optical depth effects in ^{12}CO by checking the consistency of the derived cloud dust masses.

We compute α'_{CO} for the 1G dust core sample only, as for CO line profiles with multiple peaks, it is difficult to determine whether the dust emission originates from the GMC or from unrelated structures along the line of sight. Individual dust core $\alpha'_{^{12}CO}$ values are displayed in Figure 5 and reported in Table 2. A minimum uncertainty of 0.01 is adopted. The weighted mean value of $\alpha'_{^{12}CO}$ for resolved dust cores is $0.070 \pm 0.031\ M_\odot$ (K km s^{-1} pc^2)$^{-1}$, which is in excellent agreement with the previous measurement of $0.064 \pm 0.029\ M_\odot$ (K km s^{-1} pc^2)$^{-1}$ from S. Viaene et al. (2021). The mean $\alpha'_{^{12}CO}$ values for resolved and unresolved dust cores, shown in Figure 5, are consistent within 1σ. However, for unresolved dust cores, the source size cannot be reliably determined, introducing additional uncertainty in the corresponding measurements. The uncertainties reported in the mean

Table 2
α'_{CO} for Individual 1G Dust Cores from both $L_{^{12}CO}$ and $L_{^{13}CO}$

Source	$\alpha'_{^{12}CO}$ $M_\odot$ (K km s^{-1} pc^2)$^{-1}$	$\alpha'_{^{13}CO}$ $M_\odot$ (K km s^{-1} pc^2)$^{-1}$
K001Ad1	0.04 ± 0.01	0.30 ± 0.07
K001Ad2	0.03 ± 0.01	0.15 ± 0.05
K026Ad1[a]	0.07 ± 0.01	0.34 ± 0.03
K063Ad1[a]	0.08 ± 0.01	0.56 ± 0.12
K063Ad3	0.04 ± 0.01	0.29 ± 0.10
K067Ad1[a]	0.06 ± 0.02	0.29 ± 0.08
K071Ad1[a]	0.11 ± 0.02	0.52 ± 0.10
K071Ad2	0.05 ± 0.01	0.38 ± 0.11
K081Ad1	0.06 ± 0.02	0.29 ± 0.09
K092Ad1[a]	0.09 ± 0.01	0.36 ± 0.05
K093Ad1[a]	0.10 ± 0.02	0.43 ± 0.12
K094Ad1	0.04 ± 0.01	0.21 ± 0.07
K098Ad1	0.05 ± 0.02	0.40 ± 0.15
K098Bd1[a]	0.05 ± 0.01	0.24 ± 0.04
K119Bd1[a]	0.12 ± 0.01	0.54 ± 0.05
K120Ad1[a]	0.16 ± 0.04	0.76 ± 0.21
K134Ad1	0.05 ± 0.02	0.26 ± 0.08
K134Ad2	0.06 ± 0.02	0.52 ± 0.20
K136Ad2	0.07 ± 0.02	0.39 ± 0.10
K138Ad1[a]	0.05 ± 0.01	0.27 ± 0.03
K149Ad1	0.07 ± 0.02	0.41 ± 0.13
K151Ad1	0.04 ± 0.01	0.44 ± 0.16
K153Ad1	0.03 ± 0.01	0.29 ± 0.08
K153Ad2	0.03 ± 0.01	0.29 ± 0.11
K154Ad1[a]	0.12 ± 0.02	0.74 ± 0.15
K157Bd2	0.11 ± 0.03	0.76 ± 0.24
K160Cd1	0.07 ± 0.02	0.60 ± 0.20
K162Ad1[a]	0.03 ± 0.01	0.19 ± 0.04
K162Ad2	0.04 ± 0.01	0.26 ± 0.08
K170Ad1[a]	0.05 ± 0.01	0.26 ± 0.04
K171Ad1	0.07 ± 0.02	0.30 ± 0.08
K176Ad1[a]	0.05 ± 0.01	0.28 ± 0.06
K177Ad1[a]	0.06 ± 0.02	0.27 ± 0.07
K177Ad2	0.03 ± 0.01	0.17 ± 0.04
K190Ad1[a]	0.18 ± 0.02	1.84 ± 0.28
K191Ad1[a]	0.08 ± 0.01	0.42 ± 0.08
K192Ad1	0.09 ± 0.03	0.37 ± 0.11
K213Ad1[a]	0.09 ± 0.01	0.51 ± 0.05
K239Ad2	0.03 ± 0.01	0.23 ± 0.09
K240Ad1	0.16 ± 0.05	1.05 ± 0.34
K240Bd1	0.14 ± 0.04	1.63 ± 0.62
K270Ad1[a]	0.09 ± 0.01	0.59 ± 0.06
K270Ad2	0.06 ± 0.02	0.42 ± 0.12
K275Bd1	0.12 ± 0.03	0.79 ± 0.21
K291Ad1	0.25 ± 0.05	2.20 ± 0.56
K297Ad1	0.08 ± 0.01	0.58 ± 0.06
K301Ad1[a]	0.05 ± 0.00	0.24 ± 0.03

Note.
[a] Resolved dust cores.

(This table is available in machine-readable form in the online article.)

α'_{CO} from all dust cores represent the standard deviation of the individual dust core measurements and are similar in magnitude to those found by S. Viaene et al. (2021).

Although no explicit $\alpha'_{^{12}CO}$ value has been calculated for MW GMCs, one can estimate it from the A. D. Bolatto et al. (2013) value of α_{CO} for ^{12}CO(1−0), assuming a gas-to-dust ratio of $R_{g/d} \sim 136$ and an intensity ratio of $I_{CO}(1-0)/I_{CO}(2-1) = 0.7$. This yields an MW value of $\alpha'_{^{12}CO} \sim 0.045\ M_\odot$ (K km s^{-1} pc^2)$^{-1}$ ± 0.3 dex. The value calculated here for M31 agrees within $<1\sigma$, with a smaller relative uncertainty compared to the MW estimate.

As is done for $\alpha'_{^{12}CO}$, individual $\alpha'_{^{13}CO}$ values for 1G dust cores in M31 are displayed in Figure 6 and reported in Table 2. The mean $\alpha'_{^{13}CO}$ of the resolved sources is $0.37 \pm 0.20\ M_\odot$ (K km s^{-1} pc^2)$^{-1}$, which is in excellent agreement with the previous value of $0.36 \pm 0.15\ M_\odot$ (K km s^{-1} pc^2)$^{-1}$ reported by S. Viaene et al. (2021). We see that the mean $\alpha'_{^{13}CO}$ for resolved and unresolved dust cores are again in agreement within 1σ.

In this study, we calculate α'_{CO} from dust core emission rather than from the entire GMC. The differences between values derived from dust cores within the same GMC are smaller than the overall standard deviation, indicating that these measurements are representative of entire GMCs within the uncertainties. We examined α'_{CO} variations within the best-resolved dust cores. Only marginal nominal differences were found between pixels separated by more than one beam, and smaller-scale differences are likely temperature-driven rather than true α'_{CO} variations, especially near H II regions. We therefore find no compelling evidence for significant α'_{CO} variation within dust cores.

C. J. Lada et al. (2024) found that M31 GMCs belong to one of two classes: dense and diffuse. Dense GMCs are identified by their strong ^{13}CO(2−1) emission lines. We further expect that all 1G dust cores are associated with dense GMCs, as all display measurable ^{13}CO(2−1) emission.

In dust cores K071Ad1, K119Bd1, K120Ad1, K154Ad1, and K190Ad1, the dust emission peak lies near the edge of the GMC, where CO emission is weaker. Consequently, values of $L_{^{12}CO}$ and sometimes $L_{^{13}CO}$ are lower than at the cloud center, where the peak CO emission occurs. As a result, the ratio of M_{dust}/L_{CO} is biased high. This may be due to variations in T_{dust} within the GMC. For source K190Ad1 to have $\alpha'_{^{12}CO} = 0.07\ M_\odot$ (K km s^{-1} pc^2)$^{-1}$, a T_{dust} of 38 K would be required. The other aforementioned outliers would require $25\ K \lesssim T_{dust} \lesssim 36\ K$. In Orion, T_{dust} derived from continuum emission is typically 20−30 K (e.g., M. Bouvier et al. 2021) but can be as high as $T_{dust} \lesssim 50$ K in warmer regions (Y. L. Shirley et al. 2005). In M17, T_{dust} ranges from ∼10 to 100 K (X. Dupac et al. 2002). These measurements are obtained on much smaller scales than those used in this work (<0.1 pc). Therefore, while a T_{dust} of 38 K can occur in a region heated by a nearby H II region, this is unlikely on 15 pc scales. On larger scales, Herschel observations indicate a T_{dust} range of 15–20 K for M31 GMAs (J. M. Kirk et al. 2015). Thus, variations in $\alpha'_{^{12}CO}$ between clouds may reflect T_{dust} differences; it is also possible that some dust continuum emission is not physically associated with the GMC.

4.4. Virial Analysis

Next, we performed a virial analysis of the resolved 1G dust cores in our sample to investigate the influence of gravity and turbulence on cloud dynamics. We include only 1G resolved sources in this analysis, as source radii and ^{13}CO(2−1) line widths are required to calculate the virial mass (M_{vir}) following Equation (4). C. J. Lada et al. (2024) showed that, while most M31 GMCs are unbound, the strongest ^{13}CO emission arises from bound GMCs. As discussed in Section 4.2, dust traces the densest regions within these GMCs, therefore providing additional insight into the physical conditions that govern star formation.

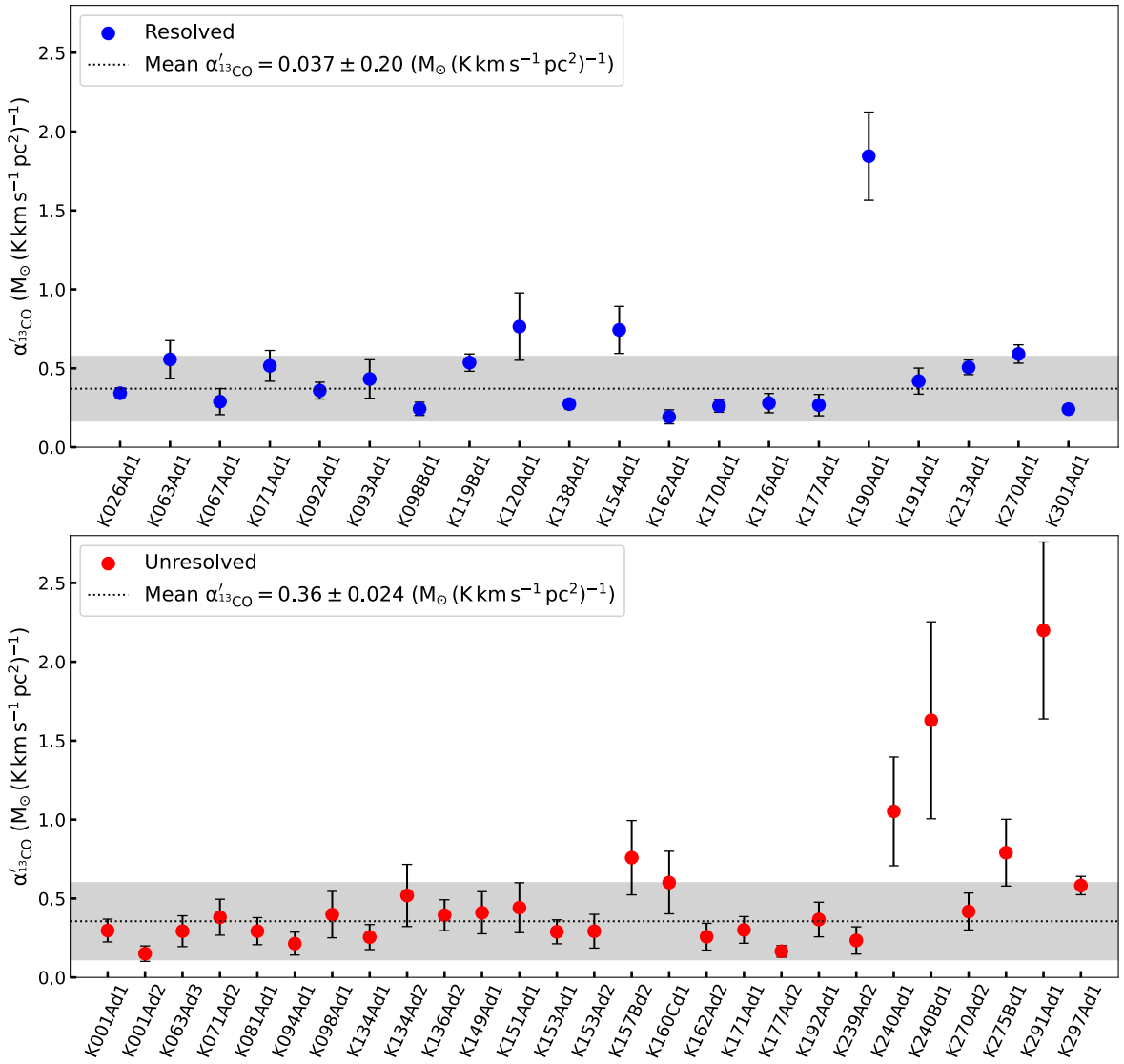

Figure 6. ^{13}CO conversion factors, $\alpha'_{^{13}CO}$, for individual 1G dust clouds for (top) resolved sources and (bottom) unresolved sources. As in Figure 5, we display the mean $\alpha'_{^{13}CO}$ calculated for resolved and unresolved sources as a dotted line, with the 1σ standard deviation represented by the shaded region.

The virial theorem, one of Larson's relations (R. B. Larson 1981), states that for a self-gravitating GMC, the kinetic energy (KE) is twice the gravitational potential energy (GPE). This implies that the internal KE from turbulence is balanced by self-gravity. Assuming a stratified cloud with an internal density gradient of $\rho(r) \propto r^{-1}$ (P. M. Solomon et al. 1987), the virial mass is then given by

$$M_{\rm vir} = 1040\ \sigma^2 R\ (M_\odot), \tag{4}$$

where σ is the velocity dispersion in km s^{-1} and R is the effective radius in parsecs.

For a virialized cloud, the virial parameter $\alpha_{\rm vir} = 2\,{\rm KE/GPE} = 1.0$. The virial nature of a system can be inferred from the relationship between $M_{\rm vir}$ and $M_{\rm lum}$, where a one-to-one scaling relation is expected for virialized clouds. R. B. Larson (1981) derived the following relation between velocity dispersion and mass: $\sigma \propto M^{0.20}$, with an rms deviation of 0.12 dex. C. J. Lada et al. (2024) found an almost identical relation for M31 GMCs using the same observations discussed here. For a virialized system, $M_{\rm vir} = M_{\rm lum}^{1.0}$ is expected (e.g., C. J. Lada et al. 2024).

The virial mass of each dust core is derived using ^{13}CO line widths for velocity dispersion, as these are more suitable than ^{12}CO line widths for this purpose, because dust and ^{13}CO are better spatially matched in our observations (see Section 4.1). $M_{\rm lum}$ is calculated using the $\alpha_{^{12}CO}$ value derived for each individual dust core and assuming $R_{\rm g/d} = 136$, multiplied by the $L_{^{12}CO}$ measured within the dust core area. This yields the dust-based gas mass of the dust core. Because both $\alpha_{\rm CO}$ and $L_{\rm CO}$ are evaluated for each individual dust core, this calculation is mathematically equivalent to $M_{\rm lum} = 136 \times M_{\rm dust}$. Consequently, identical results are obtained when using $\alpha_{^{12}CO}$ for either ^{12}CO or ^{13}CO.

Figure 7 displays the relationship between $M_{\rm vir}$ and $M_{\rm lum}$ for our 20 resolved 1G dust cores. The majority (80%) of dust cores are found to be gravitationally bound and approximately virialized. Although four dust cores lie within the unbound area of Figure 7, they all lie within approximately 1σ of the bound line and are therefore likely also bound. We note that the use of ^{13}CO line widths for σ provides upper limits for the $M_{\rm vir}$ of these dust cores, and ideally, C^{18}O line widths would be used, as this tracer has a lower optical depth.

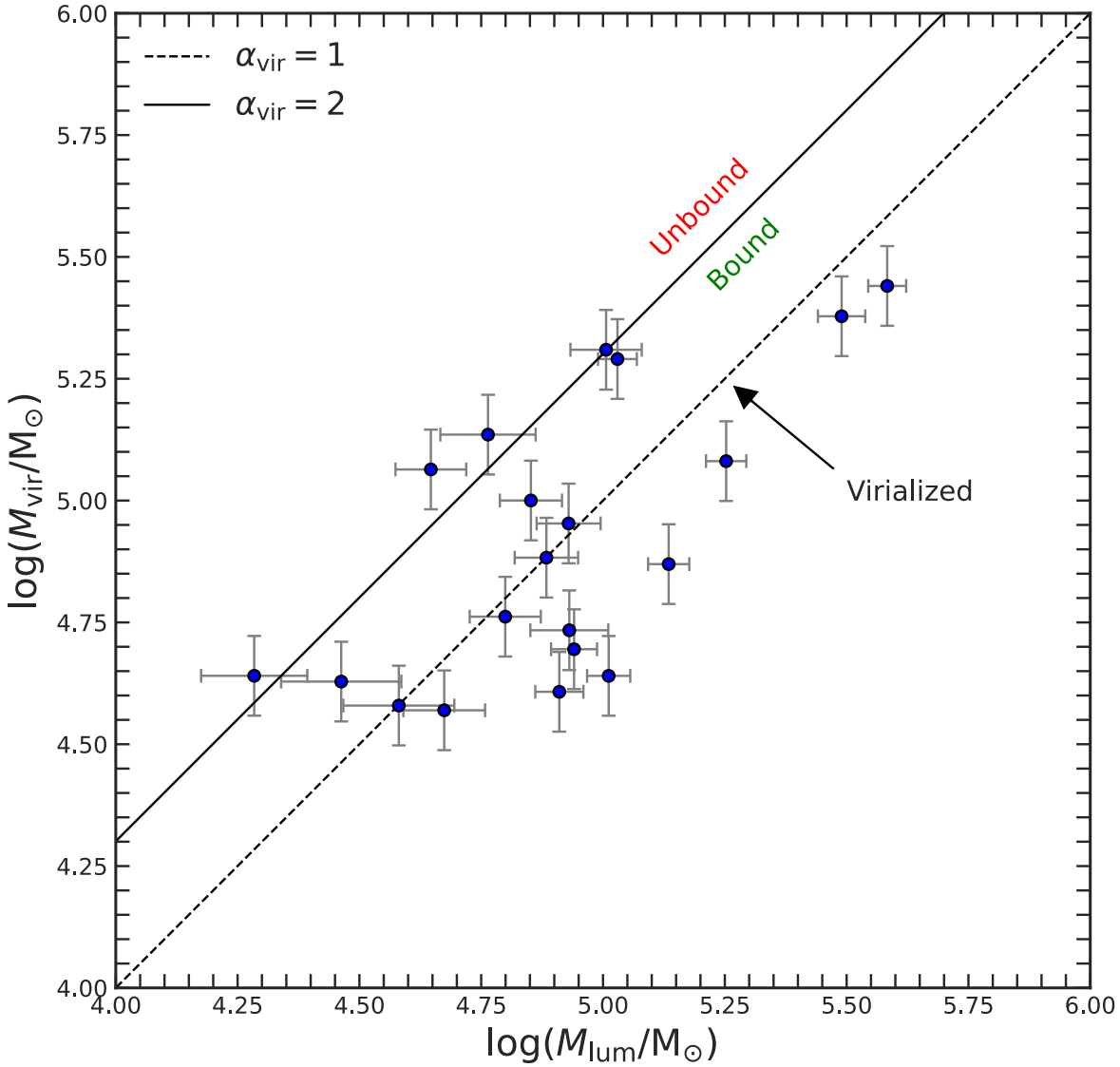

Figure 7. Comparison between the virial mass and the dust-based gas mass (both from within the 2.5σ dust continuum contour) for individual resolved dust cores in our sample.

C. J. Lada et al. (2024) present a virial analysis of M31 GMCs traced by ^{12}CO and ^{13}CO from the same dataset. While only 43% of the GMCs traced by ^{12}CO are bound, 94% of the ^{13}CO-emitting "clumps" are bound and approximately virialized (C. J. Lada et al. 2024). The results found here are consistent with those of C. J. Lada et al. (2024): while M31 GMCs appear largely unbound, the denser regions traced by dust and ^{13}CO are contained within bound GMCs that are also close to being in virial equilibrium. This is also similar to the results from N. J. Evans et al. (2021) for MW GMCs, where 70%–80% of the GMCs were found to be unbound, but 60% of the ^{13}CO regions are bound. Both N. J. Evans et al. (2021) and C. J. Lada et al. (2024) found that the bound fraction of GMCs increases with cloud mass.

4.5. Metallicity Dependence of α'_{CO}

As introduced in Section 1, we update the result presented in C. Bosomworth et al. (2025), investigating the metallicity dependence of α'_{CO}. This SMA sample contains 30 1G dust cores associated with the same GMCs as the 30 H II regions from C. Bosomworth et al. (2025). We note that the dust cores and H II regions are not necessarily spatially coincident. H II region metallicities were calculated from MMT/Hectospec optical spectroscopy. The primary metallicity trend found in M31 is a negative linear correlation with galactocentric radius, as expected for spiral galaxies (e.g., B. M. Tinsley 1980; L. J. Kewley et al. 2019; R. Maiolino & F. Mannucci 2019). α_{CO} is predicted to be higher at low metallicities (A. D. Bolatto et al. 2013) and for α'_{CO} if $R_{g/d}$ is constant. Therefore, α_{CO} may also be assumed to vary linearly with galactocentric radius.

First, both dust and CO are more abundant in higher-metallicity environments. Second, the dust mass and CO luminosity are each expected to vary independently with metallicity. Dust plays a crucial role in shielding CO from destruction by ultraviolet (UV) photons; therefore, at lower metallicities, a greater fraction of CO is destroyed by UV radiation (A. D. Bolatto et al. 2013). These combined effects may either exacerbate or mitigate variations in the ratio of M_{dust} to L_{CO}.

We display the updated relationship between α'_{CO} and O/H in Figure 8. Despite probing a significant metallicity range of ~8.40–8.65, we find that $\alpha'_{^{12}CO}$ remains approximately constant

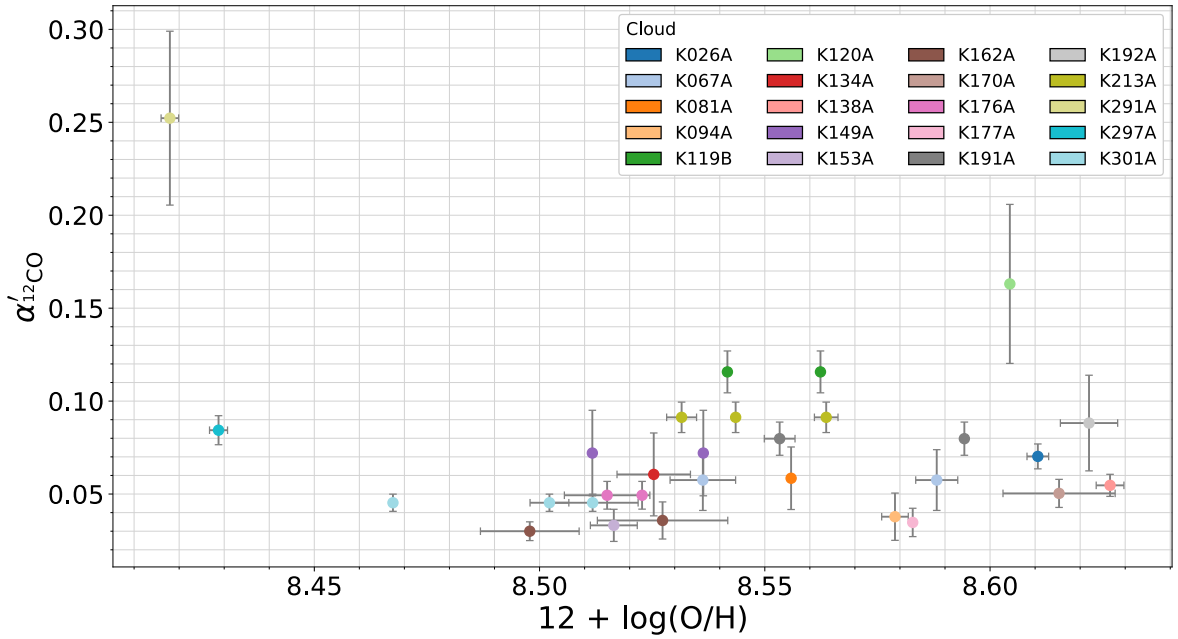

Figure 8. The variation of the CO-to-dust mass conversion factor, $\alpha'_{^{12}CO}$, with metallicity (oxygen abundance) for SMA dust detections in this work, which have at least one associated H II region identified from optical spectroscopy (C. Bosomworth et al. 2025). Some GMAs have multiple H II regions, so the data points are colored according to the associated GMA/GMC.

with a mean of $0.062 \pm 0.029\ M_\odot\ (\mathrm{K\ km\ s^{-1}\ pc^2})^{-1}$, consistent within $<2\sigma$ for most data points. The majority of sources in this sample have metallicities of $\mathrm{O/H} > 8.5$, and a significant dependence of α_{CO} on metallicity is primarily expected at $12 + \log(\mathrm{O/H}) < 8.4$. Therefore, a larger sample at lower metallicities is required to determine whether a trend in α'_{CO} exists.

Our results are consistent with a constant $\alpha'_{^{12}CO}$ across the metallicity range $8.45 < \mathrm{O/H} < 8.65$ in M31 and a constant α_{CO} if the MW value of $R_{g/d} \sim 136$ is assumed. This contrasts with theoretical predictions that α_{CO} is negatively correlated with metallicity. By probing the metallicity range $\mathrm{O/H} < 8.5$ with a sufficiently large sample size, we can better constrain the metallicity dependence of $\alpha'_{^{12}CO}$ in M31 and similar galaxies. Alternatively, it may be that $R_{g/d}$ varies with metallicity.

5. Summary and Conclusions

The recent upgrade to the SMA wideband receiver has enabled the first resolved dust continuum detections from individual GMCs in M31. Earlier studies by J. Forbrich et al. (2020) and S. Viaene et al. (2021) showed that, by using SMA observations of simultaneous CO(2–1) and 230 GHz continuum emission at ∼15 pc resolution, it is possible to derive the dust mass-to-light conversion factor (α'_{CO}) for 32 dust cores associated with M31 GMCs (10 resolved). Analysis from the initial two observing runs of the SMA survey revealed that the α'_{CO} for M31 GMCs is approximately constant and similar to that of the MW when $R_{g/d} = 136$ is assumed. In this paper, we analyze the now-completed SMA survey, consisting of four observing runs targeting 80 Herschel-identified GMAs. We increased the sample to 71 dust continuum detections (26 resolved) associated with 56 GMCs. We identified a subsample of 47 1G dust cores with CO line profiles well represented by a single Gaussian (20 resolved). We calculated α'_{CO} for both ^{12}CO and ^{13}CO for the 1G sample, then performed an assessment of whether the resolved 1G dust cores are gravitationally bound and/or virialized. Finally, we updated the test of the metallicity dependence of α'_{CO} using H II region metallicities presented in C. Bosomworth et al. (2025).

1. We reanalyzed the entire dataset using a dust emission detection threshold of 2.5σ and limited the final sample to sources associated with GMCs defined by ^{12}CO emission, identifying new detections in the original two observing runs as well as in the new observations. The defined 1G subsample consists of sources with single-component line profiles in both ^{12}CO(2−1) and ^{13}CO(2−1), thus eliminating confusion due to overlapping emission.
2. We calculated the CO-to-dust mass conversion factor, α'_{CO}, for 47 1G dust cores. The mean values derived from the sample of 20 resolved sources are $\langle\alpha'_{^{12}CO}\rangle = 0.070 \pm 0.031\ M_\odot\ (\mathrm{K\ km\ s^{-1}\ pc^2})^{-1}$ and $\langle\alpha'^{13}\mathrm{CO}\rangle = 0.37 \pm 0.20\ M_\odot\ (\mathrm{K\ km\ s^{-1}\ pc^2})^{-1}$. These values are in excellent agreement with those previously reported by J. Forbrich et al. (2020) and S. Viaene et al. (2021).
3. Assuming an MW value of $R_{g/d} = 136$, the corresponding CO-to-cloud mass conversion factor is $\langle\alpha_{^{12}CO}\rangle_{M31} = 9.52 \pm 4.22\ M_\odot\ (\mathrm{K\ km\ s^{-1}\ pc^2})^{-1}$. The corresponding MW value is $\langle\alpha_{^{12}CO}\rangle_{MW} = 6.1\ M_\odot\ (\mathrm{K\ km\ s^{-1}\ pc^2})^{-1}$, derived from the A. D. Bolatto et al. (2013) value for CO(1–0). $\langle\alpha_{^{12}CO}\rangle_{M31}$ agrees with the MW value within 1σ uncertainties. Our uncertainty estimate is comparable to that recommended by A. D. Bolatto et al. (2013) for the MW but has a smaller relative uncertainty and is statistically derived.
4. We find that 80% of the dust cores are gravitationally bound (i.e., $|\mathrm{GPE}| > \mathrm{KE}$). Moreover, all sources lie within 1σ of the gravitationally bound condition. This is consistent with the findings of C. J. Lada et al. (2024), who reported that M31 GMCs are largely unbound but that dense gas regions (identified from ^{13}CO emission) are contained within bound GMCs. Our results therefore suggest that the dust cores are located within these bound GMCs.

5. Finally, we update the C. Bosomworth et al. (2025) test of $\alpha'_{\rm CO}$ variation with metallicity (O/H). Despite the significant range of metallicities probed, we find no evidence of $\alpha'_{^{12}\rm CO}$ dependence on metallicity across the range $8.45 \lesssim {\rm O/H} \lesssim 8.65$.

Acknowledgments

The Submillimeter Array is a joint project between the Smithsonian Astrophysical Observatory and the Academia Sinica Institute of Astronomy and Astrophysics and is funded by the Smithsonian Institution and the Academia Sinica. C.B. acknowledges funding from a predoctoral fellowship at Center for Astrophysics | Harvard & Smithsonian.

Facility: SMA.

Software: Astropy (Astropy Collaboration et al. 2013, 2018, 2022), APLpy (T. Robitaille & E. Bressert 2012; T. Robitaille 2019).

Appendix
SMA Dust Nondetections Source Catalog

In Figure 9 we present the dust continuum images of the 26 observed GMAs which do not contain any dust cores.

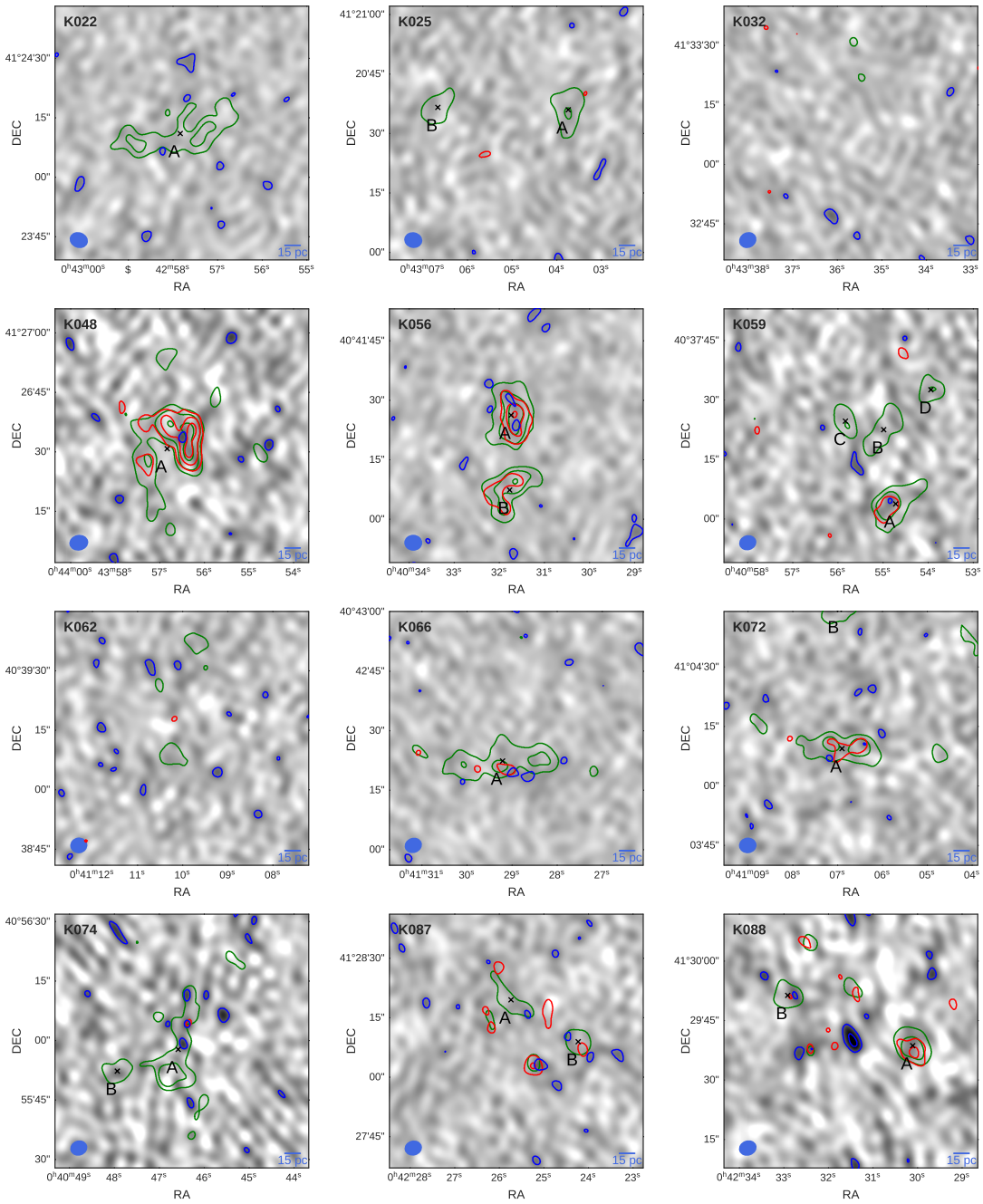

Figure 9. SMA maps of the dust continuum of individual (J. M. Kirk et al. 2015) GMAs in M31 for clouds that contain no dust cores. Blue contours display dust continuum emission at 2.5σ, 3.5σ, and 4.5σ. Green contours display ^{12}CO at 3σ, 6σ, 12σ, 24σ, and 48σ. Red contours display ^{13}CO at 3σ, 6σ, and 10σ. The corresponding centers of mass (by area) of individual GMCs as traced by ^{12}CO at 3σ are marked by black crosses.

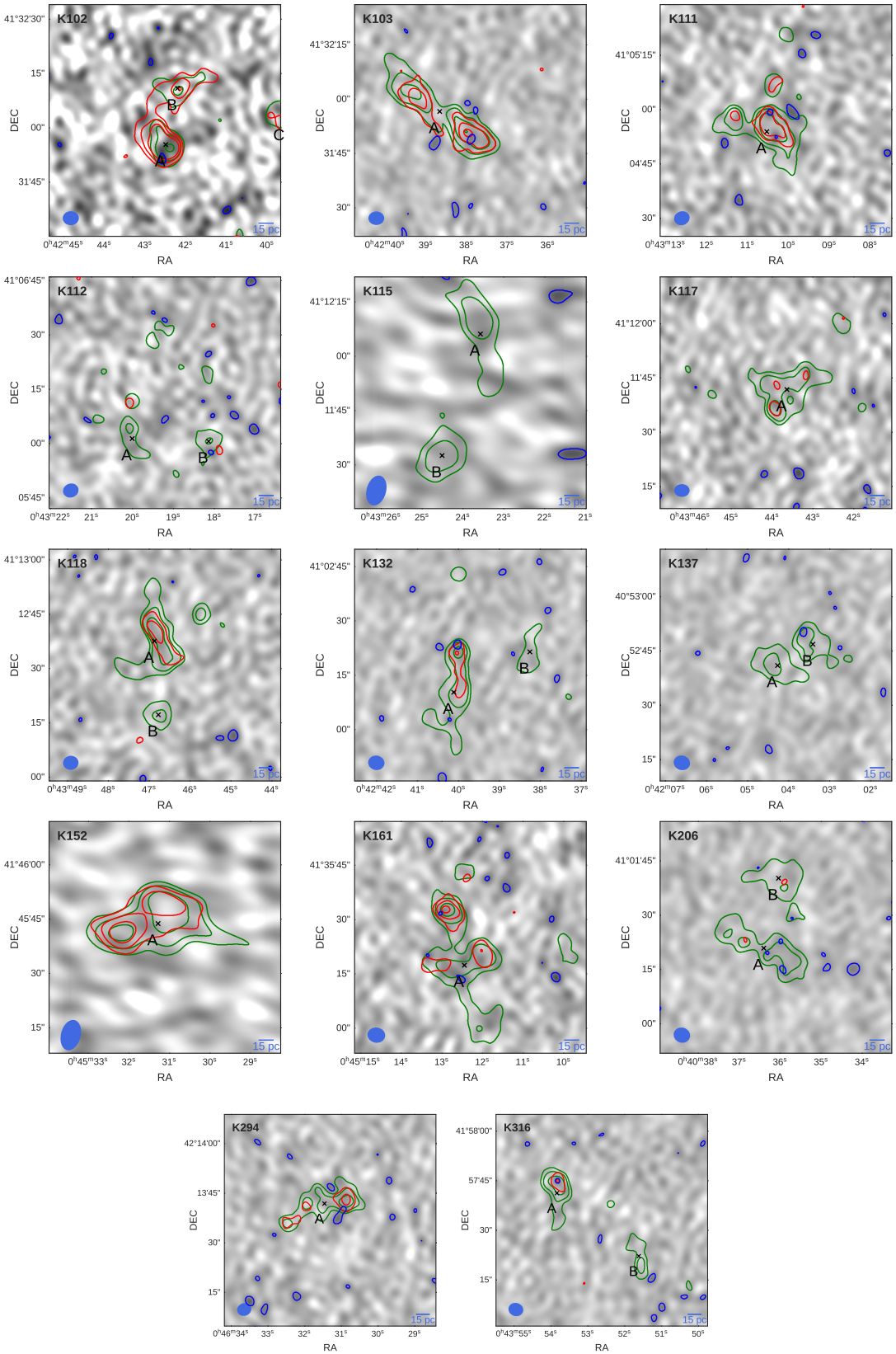

Figure 9. (Continued.)

ORCID iDs

Chloe Bosomworth https://orcid.org/0009-0007-9655-7151
Jan Forbrich https://orcid.org/0000-0001-8694-4966
Charles J. Lada https://orcid.org/0000-0002-4658-7017

References

Alves, J., Lada, C., & Lada, E. 2001, Natur, 409, 159
Astropy Collaboration, Price-Whelan, A. M., Lim, P. L., et al. 2022, ApJ, 935, 167
Astropy Collaboration, Price-Whelan, A. M., Sipőcz, B. M., et al. 2018, AJ, 156, 123
Astropy Collaboration, Robitaille, T. P., Tollerud, E. J., et al. 2013, A&A, 558, A33
Bolatto, A. D., Wolfire, M., & Leroy, A. K. 2013, ARA&A, 51, 207
Bosomworth, C., Forbrich, J., Lada, C. J., et al. 2025, MNRAS, 536, 3803
Bouvier, M., López-Sepulcre, A., Ceccarelli, C., et al. 2021, A&A, 653, A117
Colombo, D., Hughes, A., Schinnerer, E., et al. 2014, ApJ, 784, 3
Dame, T. M., & Lada, C. J. 2023, ApJ, 944, 197
Draine, B. T., Dale, D. A., Bendo, G., et al. 2007, ApJ, 663, 866
Dupac, X., Giard, M., Bernard, J. P., et al. 2002, A&A, 392, 691
Evans, N. J., Heyer, M., Miville-Deschênes, M.-A., Nguyen-Luong, Q., & Merello, M. 2021, ApJ, 920, 126
Faesi, C. M., Lada, C. J., & Forbrich, J. 2018, ApJ, 857, 19
Forbrich, J., Lada, C. J., Pety, J., & Petitpas, G. 2023, MNRAS, 525, 5565
Forbrich, J., Lada, C. J., Viaene, S., & Petitpas, G. 2020, ApJ, 890, 42
Fritz, J., Gentile, G., Smith, M. W. L., et al. 2012, A&A, 546, A34
Gao, Y., & Solomon, P. M. 2004, ApJ, 606, 271
Giannetti, A., Leurini, S., König, C., et al. 2017, A&A, 606, L12
Glover, S. C. O., & Clark, P. C. 2012, MNRAS, 421, 116
Glover, S. C. O., Federrath, C., Mac Low, M. M., & Klessen, R. S. 2010, MNRAS, 404, 2
Goodman, A. A., Pineda, J. E., & Schnee, S. L. 2009, ApJ, 692, 91
Gordon, K. D., Bailin, J., Engelbracht, C. W., et al. 2006, ApJL, 638, L87
Grimes, P., Blundell, R., Paine, S., Tong, C. Y. E., & Zeng, L. 2016, SPIE, 9914, 991424
Heyer, M., & Dame, T. 2015, ARA&A, 53, 583
Hildebrand, R. H. 1983, QJRAS, 24, 267
Hirashita, H., & Harada, N. 2017, MNRAS, 467, 699
Israel, F. P. 1997, A&A, 328, 471
Jones, A., Köhler, M., Ysard, N., Bocchio, M., & Verstraete, L. 2017, A&A, 602, A46
Kewley, L. J., Nicholls, D. C., & Sutherland, R. S. 2019, ARA&A, 57, 511
Kirk, J. M., Gear, W. K., Fritz, J., et al. 2015, ApJ, 798, 58
Lada, C. J., Forbrich, J., Lombardi, M., & Alves, J. F. 2012, ApJ, 745, 190
Lada, C. J., Forbrich, J., Petitpas, G., & Viaene, S. 2024, ApJ, 966, 193
Lada, C. J., Lada, E. A., Clemens, D. P., & Bally, J. 1994, ApJ, 429, 694
Lada, C. J., Lombardi, M., & Alves, J. F. 2010, ApJ, 724, 687
Lada, C. J., Margulis, M., Sofue, Y., Nakai, N., & Handa, T. 1988, ApJ, 328, 143
Larson, R. B. 1981, MNRAS, 194, 809
Leroy, A. K., Bolatto, A., Gordon, K., et al. 2011, ApJ, 737, 12
Leroy, A. K., Schinnerer, E., Hughes, A., et al. 2021, ApJS, 257, 43
Madau, P., & Dickinson, M. 2014, ARA&A, 52, 415
Maiolino, R., & Mannucci, F. 2019, A&ARv, 27, 3
Maloney, P. 1988, ApJ, 334, 761
Mattsson, L., & Andersen, A. C. 2012, MNRAS, 423, 38
Pety, J., Guzmán, V. V., Orkisz, J. H., et al. 2017, A&A, 599, A98
Rice, T. S., Goodman, A. A., Bergin, E. A., Beaumont, C., & Dame, T. M. 2016, ApJ, 822, 52
Robitaille, T. 2019, APLpy v2.0: The Astronomical Plotting Library in Python, v2.0, Zenodo, doi:10.5281/zenodo.2567476
Robitaille, T., & Bressert, E. 2012, APLpy: Astronomical Plotting Library in Python, Astrophysics Source Code Library, ascl:1208.017
Saintonge, A., & Catinella, B. 2022, ARA&A, 60, 319
Sandstrom, K. M., Leroy, A. K., Walter, F., et al. 2013, ApJ, 777, 5
Savage, B. D., & Sembach, K. R. 1996, ARA&A, 34, 279
Scoville, N., Lee, N., Vanden Bout, P., et al. 2017, ApJ, 837, 150
Scoville, N., Sheth, K., Aussel, H., et al. 2016, ApJ, 820, 83
Shirley, Y. L., Nordhaus, M. K., Grcevich, J. M., et al. 2005, ApJ, 632, 982
Solomon, P. M., Rivolo, A. R., Barrett, J., & Yahil, A. 1987, ApJ, 319, 730
Solomon, P. M., Sanders, D. B., & Scoville, N. Z. 1979, IAUS, 84, 35
Stanek, K. Z., & Garnavich, P. M. 1998, ApJL, 503, L131
Tacconi, L. J., Genzel, R., & Sternberg, A. 2020, ARA&A, 58, 157
Tinsley, B. M. 1980, FCPh, 5, 287
Viaene, S., Baes, M., Tamm, A., et al. 2017, A&A, 599, A64
Viaene, S., Forbrich, J., Lada, C. J., Petitpas, G., & Faesi, C. 2021, ApJ, 912, 68
Vogel, S. N., Boulanger, F., & Ball, R. 1987, ApJL, 321, L145
Wakelam, V., Bron, E., Cazaux, S., et al. 2017, MolAs, 9, 1
Ysard, N., Köhler, M., Jones, A., et al. 2015, A&A, 577, A110